FULL PAPER

Open Access

CrossMark

Magnetic ripples observed by Swarm satellites and their enhancement during typhoon activity

Tadashi Aoyama[*], Toshihiko Iyemori and Kunihito Nakanishi

Abstract

The Swarm satellites observed small-amplitude (0.1–5 nT) magnetic fluctuations perpendicular to the geomagnetic field. These so-called magnetic ripples (MRs) have a period of around a few tens of seconds along the satellite orbit in the topside ionosphere at middle and low latitudes. They are spatial structures from small-scale field-aligned currents. We investigated the following three characteristics of the MRs. First, we used Swarm observations to confirm their basic characteristics obtained from the Challenging Minisatellite Payload satellite. That is, the global distribution of the average MR amplitudes has clear geographic, seasonal, and local time dependence that is highly correlated with ionospheric conductivities. Second, we found that the average amplitudes of the MRs derived from the Swarm-B satellite, which flies at a ~50 km higher altitude, are slightly smaller than those of the Swarm-A and Swarm-C. This difference suggests that the location of the origin of MRs is below ~460 km altitude, i.e., not in the magnetosphere. Last, to provide evidence of correlation between the MRs and meteorological phenomena, we performed statistical and event analyses with typhoon track data, which are a source of acoustic and gravity waves. The data from 54 typhoons during the period from November 26, 2013, to July 31, 2016, were used for statistical analysis. The results show that the average amplitudes of the MRs during typhoon activity on the dawn, dusk, and night sides are larger than those during non-typhoon conditions. Event analyses indicate amplitude enhancements of the MRs around typhoons, and the latitude of the enhancement migrated with the typhoon. These analyses indicate that typhoon activity is correlated with MR activity and that cumulus convection activity other than typhoons may also affect MR amplitudes.

Keywords: Magnetic ripple, Magnetic fluctuation, Field-aligned current, Ionospheric dynamo, Acoustic wave, Gravity wave, Typhoon, Tropical cyclone, Swarm satellites, Cumulus convection

Introduction

Magnetic ripples (MRs) are small-amplitude (0.1–5 nT) magnetic fluctuations perpendicular to the geomagnetic field with a period of a few tens of seconds along the satellite path at middle and low latitudes in the topside ionosphere, as observed by low earth orbit (LEO) satellites. They were first reported by Nakanishi et al. (2014) and termed MRs in Aoyama et al. (2016). Nakanishi et al. (2014) observed and recorded the basic characteristics and morphology of MRs, such as the geographic, seasonal, and local time (LT) dependencies, with data obtained from the LEO satellite, Challenging Minisatellite

Payload (CHAMP). Iyemori et al. (2015) showed that they are a spatial structure from small-scale field-aligned currents (FACs) and estimated the main wave period as 200–340 s, i.e., in the range of acoustic waves, using magnetic field data obtained from the Swarm satellites. Aoyama et al. (2016) investigated the MRs and ground magnetic and GPS-TEC (Total Electron Content) variations during a volcanic eruption and showed that they are closely related.

The Swarm satellites were launched by the European Space Agency (ESA) on November 22, 2013. The three Swarm satellites were equipped with high-precision magnetometers and were almost identical to those onboard CHAMP managed by the GeoForschungsZentrum Potsdam (GFZ). They also flew in the same orbit in their

*Correspondence: aoyama@kugi.kyoto-u.ac.jp
Graduate School of Science, Kyoto University, Kyoto, Japan

Aoyama *et al. Earth, Planets and Space* (2017) 69:89

Page 2 of 21

initial phase, which was suitable for Iyemori et al. (2015) to estimate the time scale of temporal variations in MRs.

As for their origin, Nakanishi et al. (2014) suggested the possibility of the lower atmospheric disturbances, but they did not show a correspondence with any specific phenomena in the lower atmosphere. The effect of equatorial plasma bubbles (EPBs) (Stolle et al. 2006; Park et al. 2009) included on the night side might result in their occurrence to some extent. However, the Pc3 micropulsation induced from magnetosonic waves from solar wind or magnetospheric disturbances do not statistically contribute to the MR amplitude distribution (Nakanishi et al. 2014). It has been theoretically confirmed that FACs in the ionosphere can be generated from acoustic waves originating in the lower atmosphere (Zettergren and Snively 2013, 2015).

Four-minute geomagnetic and/or barometric oscillations after the 2004 Sumatra, 2007 Mieken-Chubu, 2008 Iwate-Miyagi Nairiku, and 2010 Chile earthquakes were observed in previous studies (Iyemori et al. 2005, 2013). Previous researchers have claimed that the acoustic waves propagated vertically to the ionosphere and were reflected back to the ground. That is, the vertical acoustic resonances occurred after the earthquakes, and generated an ionospheric dynamo above the epicenter (see Fig. 11 in Iyemori et al. 2013). The numerical simulation performed in Zettergren et al. (2017) supports these observations.

Aoyama et al. (2016) have shown that the acoustic waves induced from a volcanic eruption propagate to the ionosphere and generate the 4-min oscillations in the TEC and geomagnetic field and, at the same time, the MRs. The geomagnetic oscillation and the MRs are likely the results of an ionospheric E-layer dynamo. However, this was only an event analysis. In this study, we perform statistical and event analyses to investigate the effect of typhoons on MR amplitudes. A typhoon is a lower atmospheric disturbance and consists of cumulus convection activities and spiral rain bands.

In previous studies, the ionospheric response to typhoons has been detected with HF Doppler shift observations (e.g., Huang et al. 1985; Xiao et al. 2007), VLF/LF signal observations (e.g., Rozhnoi et al. 2014), and from measuring TEC (e.g., Polyakova and Perevalova 2011, 2013). Concentric wave structures associated with tropical cyclones (TCs) have been detected in mesospheric airglow images (e.g., Suzuki et al. 2013; Akiya et al. 2014; Yue et al. 2014). Typhoon-generated gravity waves have been observed using MU (Middle and Upper atmosphere) radar in the stratosphere (e.g., Sato 1993; Dhaka 2003). Some gravity waves propagate well into the thermosphere, while many gravity waves dissipate or reflect

near the mesopause. However, it is widely accepted that acoustic waves with a period less than about 4 min can propagate up to the thermosphere. Therefore, acoustic and gravity waves induced by typhoons can propagate into the upper troposphere, stratosphere, mesosphere, and thermosphere.

As the first step in this study, we confirm the seasonal and LT dependence of the global distribution of average MR amplitudes using 1 Hz magnetic field vector data from the Swarm satellites. We follow the approach of Nakanishi et al. (2014), who used data from the CHAMP satellite. Then, the difference in amplitude of the MR global distribution between satellites at different altitudes is shown. Finally, we show that the TC, termed a "typhoon" in the western Pacific Ocean in the northern hemisphere, is correlated with MR activity.

Data and method
Magnetic field vector data from Swarm satellites
The Swarm constellation consists of three satellites (SW-A, SW-B and SW-C) placed in two different polar orbits, i.e., SW-A and SW-C fly at a constant speed of ~7.5 km/s side by side (~1.40° separation in longitude) at an altitude of ~470 km, while SW-B has been at ~510 km since April 17, 2014. The main objective of the Swarm mission is to survey the geomagnetic field and its temporal evolution. The detailed specifics of the Swarm project are described in Olsen et al. (2013), and the data are provided by the ESA (https://earth.esa.int/web/guest/swarm/data-access). The 1 Hz vector magnetic field data in the sensor coordinate system are used in this study.

The procedure for data processing is the same as that used in Aoyama et al. (2016). To remove the large-scale variations, such as the geomagnetic main field, crustal anomaly, and magnetospheric currents, we first apply a third-order Savitzky-Golay smoothing filter of length 51 s to each component of the magnetic field in the sensor coordinate system within 60°N–60°S geographic latitude; the filter length corresponds to ~300 km along the satellite orbit. The smoothed data are subtracted from the observed data to obtain the small-scale geomagnetic fluctuations, including the MRs.

The local magnetic field (LMG) coordinate system is used in this paper. The "parallel" component is along the observed magnetic field, the "meridional" component is on the magnetic meridian plane and perpendicular to the parallel component (positive inward), and the "zonal" component is along a vector product of the parallel and meridional component (positive eastward). We transform each component of the small-scale fluctuations from the spacecraft sensor coordinate system (x, y, z) into the LMG coordinate system (X, Y, Z) (X: parallel, Y:

Aoyama *et al. Earth, Planets and Space* (2017) 69:89

Page 3 of 21

meridional, *Z*: zonal) assuming that the *x*-, *y*-, and *z*-axes approximately point up (or down), east (or west) and north (or south), respectively.

To define the amplitude of the MR for statistical analyses, we followed the scheme of Nakanishi et al. (2014). That is, if $\delta B_x(t)$ is a component of the magnetic fluctuation at time t, the amplitude of the MRs within a 5° latitudinal range is defined by the standard deviation of $\delta B_x(t)$ within the 5° range.

A data point outlier, where $|\delta B_x(t)| > 50$ nT, is regarded as artificial noise and removed from analysis because variations larger than 50 nT over 20–30 s are rare phenomena at the middle or low latitudes. We use a bin of 5° × 5° in geographic latitude and longitude, respectively, and average the amplitudes in each bin.

Infrared brightness temperature data from meteorological satellites

A data set of infrared (IR) brightness temperature, which is obtained from the National Centers for Environmental Prediction/National Center for Atmospheric Research (NCEP/NCAR), is a globally merged (60°N–60°S) data set from all available geostationary satellites (GOES-8/10, METEOSAT-7/5, and GMS). Time and spatial resolutions are 30 min and 4 km, respectively. The global IR composites are available in digital form via FTP (ftp://disc2.nascom.nasa.gov/data/s4pa/TRMM_ANCILLARY/MERG/).

Best track data for typhoons

Best track data consist of the positions and intensities during the life cycle of a TC, i.e., a typhoon. The data set for typhoons in the western Pacific Ocean in the northern hemisphere and South China Sea is provided by the Japan Meteorological Agency (http://www.jma.go.jp/jma/jma-eng/jma-center/rsmc-hp-pub-eg/besttrack.html). A list of the number of the typhoon occurrences for each month between December 2013 and July 2016 is provided in Table 1.

Confirmation of previous climatological results

In this section, we use Swarm magnetic field data to confirm the previous climatological (morphological) results obtained by Nakanishi et al. (2014) with the CHAMP magnetic field data. Figure 5 in Nakanishi et al. (2014) shows the LT distributions of the average amplitudes of the meridional and zonal components. In addition, Fig. 10 shows the seasonal and longitudinal distributions of the average amplitudes of the zonal component, which is generally larger than that of the meridional component, in each bin. Figure 1 presents the global distributions of average amplitudes of the zonal component in each bin within each LT sector, as observed by all three Swarm satellites within the time period from November

Table 1 Number of typhoon occurrences from December 2013 to July 2016

	2013	2014	2015	2016
Jan	–	2	1	0
Feb	–	1	1	0
Mar	–	0	2	0
Apr	–	2	1	0
May	–	0	2	0
Jun	–	2	2	0
Jul	–	5	4	4
Aug	–	1	3	–
Sep	–	5	6	–
Oct	–	2	3	–
Nov	–	2	1	–
Dec	0	1	1	–

26, 2013, to July 31, 2016. Each panel corresponds to the dawn side (3–9 LT), day side (9–15 LT), dusk side (15–21 LT), and night side (21–3 LT), respectively. Note that the horizontal and vertical axes in our Fig. 1 are geographic longitude and latitude, while those in Fig. 5 of Nakanishi et al. (2014) are dipole longitude and latitude. The bin size used in this study is 5° × 5° in geographic latitude and longitude, and the color represents the average amplitudes of the magnetic fluctuations in each bin. A 3 × 3 pixel median filter has been applied to the distribution to draw smooth image contours. The white dotted lines indicate the dipole latitudes. The bright area above ~50° in dipole latitude should be ignored because they are produced using the high-latitude FACs generated in the magnetosphere (e.g., Sugiura et al. 1982; Iyemori et al. 1985; Ishii et al. 1992; Lühr et al. 2015).

Figure 2 presents the global distributions of average amplitudes of the zonal component in each bin within each season, with the same format as shown in Fig. 1. The data are divided into the three seasons used in Park et al. (2015), the combined equinox (January 14–May 25, and July 19–November 28), June solstice (April 16–August 26), and December solstice (October 16–February 25). Swarm satellites cover all LT sectors within each season divided as indicated.

We confirm that the climatology in each LT sector or season observed by the Swarm satellites has almost the same characteristics as those observed by the CHAMP satellite. That is (1) the amplitudes of both the meridional and zonal components around the dip equator are much smaller than those at other latitudes, except for the Brazilian anomaly sector, as shown in Figs. 1 and 2 (figures of the meridional component are not shown), (2) the amplitude on the day side (~0.7 nT maximum) is much larger than that on other LT sectors (~0.2 nT maximum on the
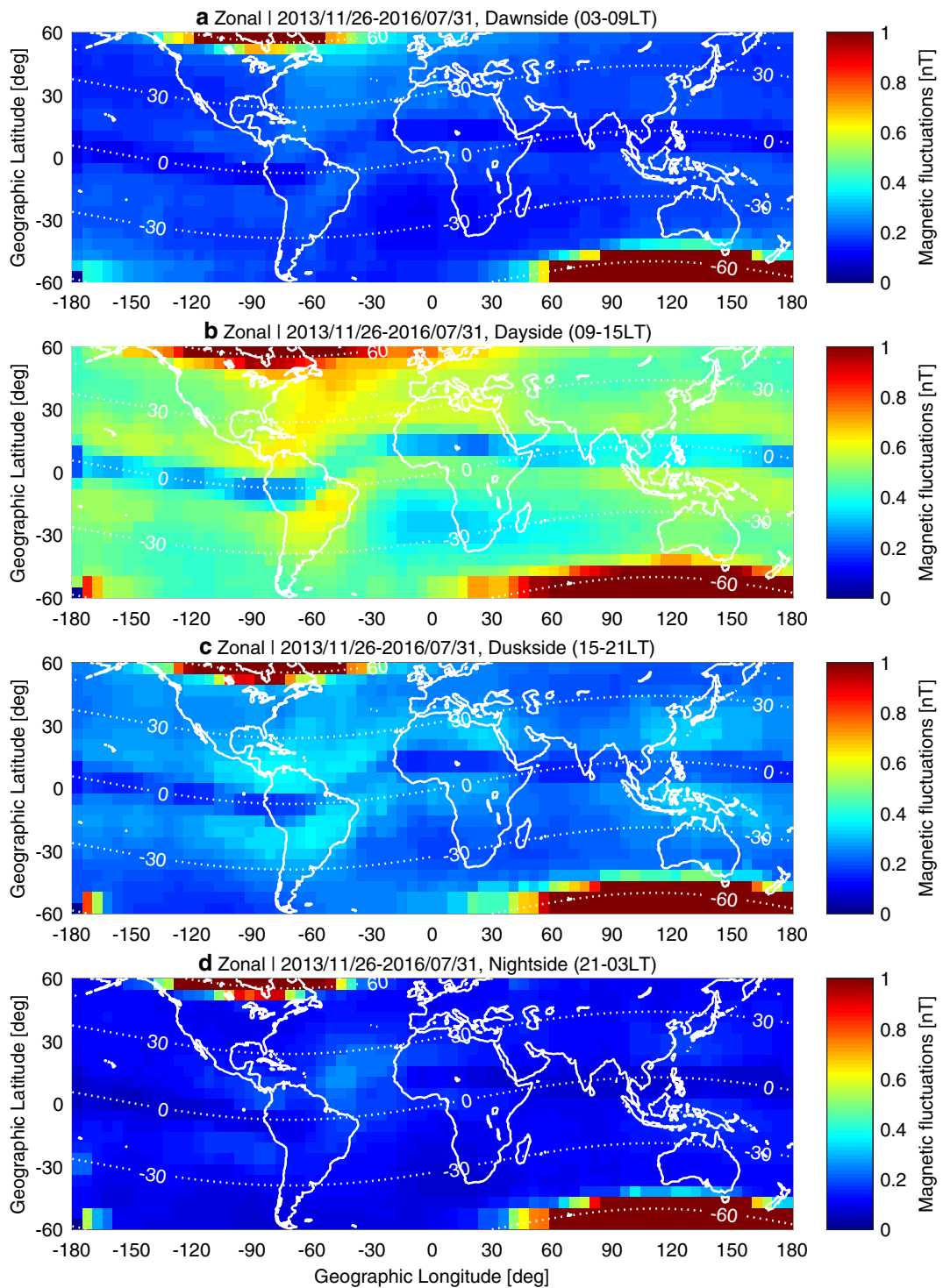
Aoyama *et al. Earth, Planets and Space* (2017) 69:89

Page 4 of 21

Fig. 1 LT dependence of the average MR amplitude distribution as observed by SW-A, SW-B, and SW-C. **a** Dawn side (3–9 LT), **b** day side (9–15 LT), **c** dusk side (15–21 LT) and **d** night side (21–3 LT)
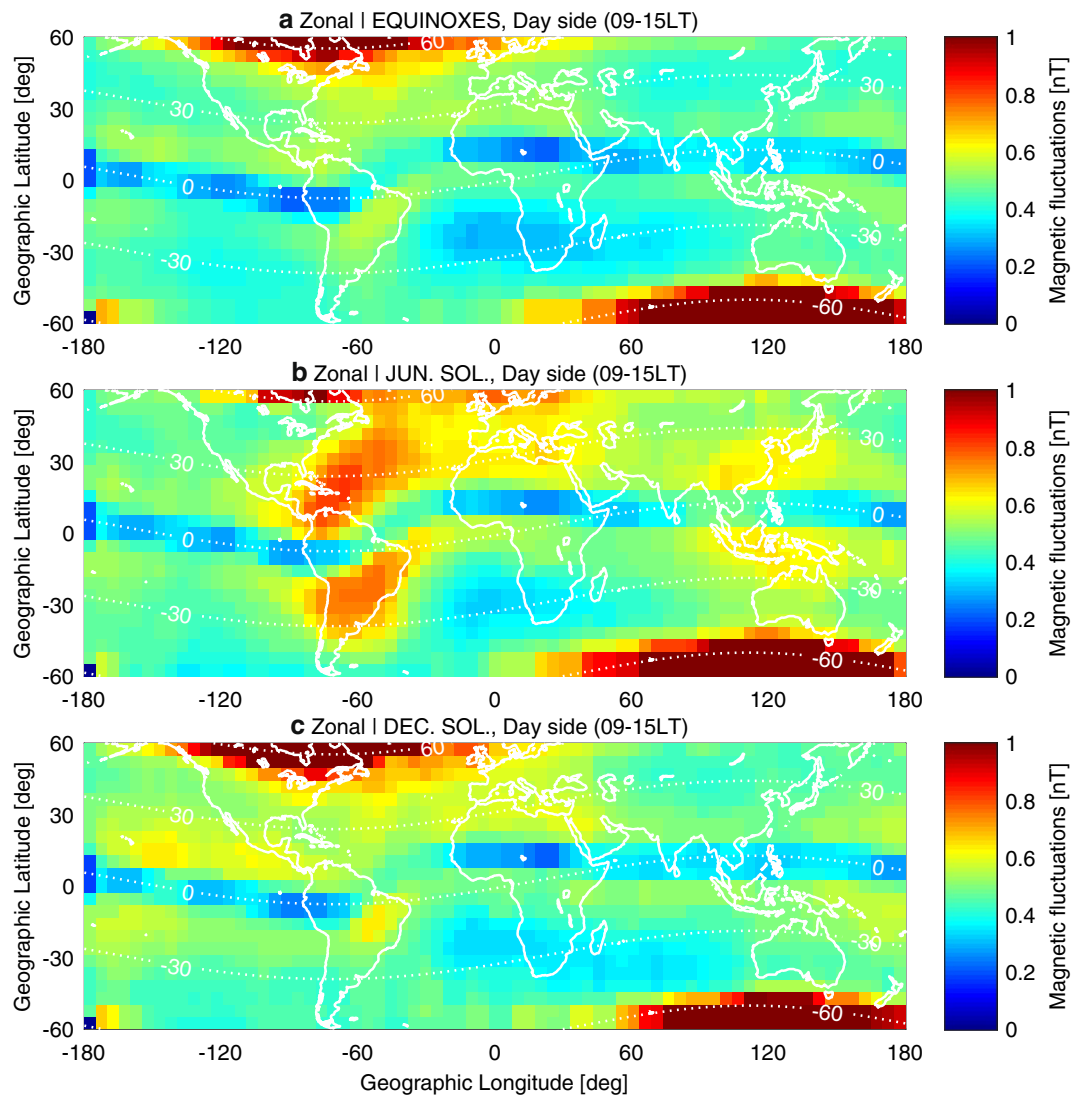
Aoyama *et al. Earth, Planets and Space* (2017) 69:89

Page 5 of 21

Fig. 2 Seasonal dependence of the MR amplitude distribution of the zonal component on the day side (9–15 LT). **a** Combined equinox, **b** June solstice and **c** December solstice

night side), (3) the amplitude on the dusk side (~0.4 nT maximum) is slightly larger than that on the dawn side (~0.3 nT maximum), (4) the amplitude during the combined equinox (~0.6 nT maximum on the day side) is less than those during the June (~0.9 nT maximum on the day side) and December (~0.7 nT maximum on the day side) solstices, (5) during the June solstice, the amplitudes above the South American Continent (~2.3 times larger than the minimum on the day side), African Continent, East Asia, and Oceania (~1.8 times larger than the minimum on the day side) are larger, (6) during the December solstice, the MRs above the Eastern Pacific Ocean are larger (~1.8 times larger than the minimum on the day side). These results are almost identical to those reported by Nakanishi et al. (2014). Characteristic (3) might be due
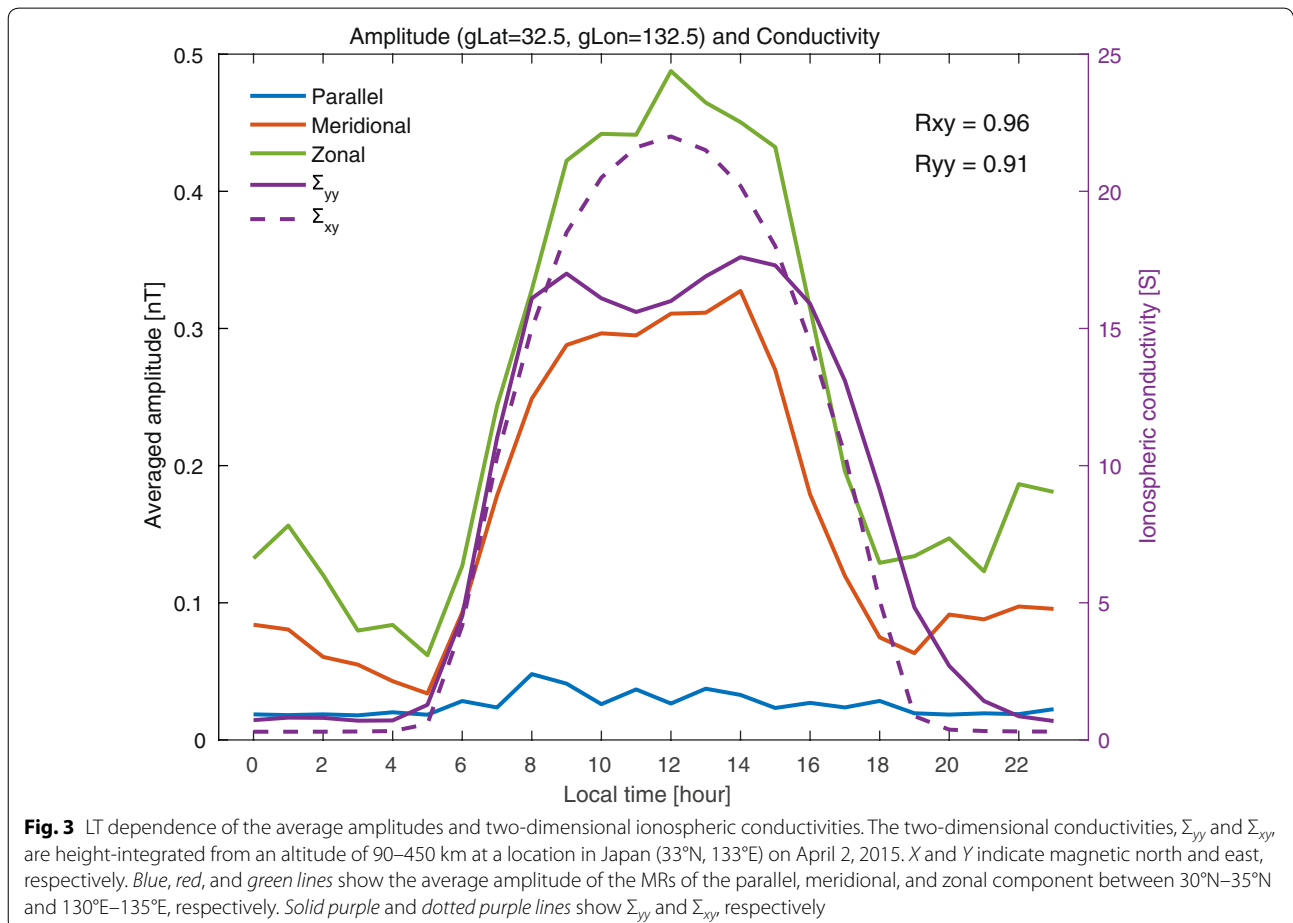
to the asymmetry of the ionospheric conductivity and/or that of the atmospheric convection activity, and/or the effect of the EPB after sunset, as described in the following text.

As indicated in "Introduction", the generation mechanism for MRs has been hypothesized to be the ionospheric E and/or F layer dynamo resulting from acoustic and/or gravity waves generated by lower atmospheric disturbances. The MR spatial scale size in the latitudinal direction is ~100 km (Nakanishi et al. 2014). According to Fig. 13 in Saito et al. (1995), electric field structures larger than ~8 km in size at the ionosphere are not attenuated much at the opposite hemisphere throughout the field line. A size of 100 km is long enough to not be short-circuited on the way to the opposite hemisphere.

Aoyama *et al. Earth, Planets and Space* (2017) 69:89

Page 6 of 21

Therefore, we consider that the FAC strength is proportional to both the ionospheric E or F layer dynamo electric field and conductivity. Figure 3 shows two important observations. First, the LT dependence of the average amplitude of each component in the northern spring (March–May) is shown in 2014, 2015, and 2016 for the area 30°N–35°N and 130°E–135°E in geographic latitude and longitude (scale shown on the left axis). Second, the height-integrated ionospheric conductivities from an altitude of 90–450 km (the lower satellites altitude) on April 2, 2015, are shown for a location (33°N, 133°E) derived from International Reference Ionosphere () (Bilitza et al. 2014) and NRLMSISE-00 model (Picone et al. 2002) (scale shown on the right axis). This figure is similar to Fig. 14 in Nakanishi et al. (2014), except for the integration height, to discuss the night side LT sector where the conductivities in the ionospheric F layer cannot be negligibly small relative to that in the E-layer. We compare MR amplitudes and two-dimensional layered conductivities, Σ_{yy} and Σ_{xy}. Here, *X* and *Y* indicate magnetic north and east, respectively. A valley is observed around noon in Σ_{yy} in our Fig. 3, which is different from Fig. 14 in Nakanishi et al. (2014). This characteristic may have come from

the phenomenon called "Midday Bite-Out event of the F2-layer" where the electron density is anomalously depressed at middle and low latitudes in the daytime due to a poleward neutral wind (Saryo et al. 1989). We note that the LT variation of the meridional component of average MR amplitude shows a similar "bite out" around noon. Nakanishi et al. (2014) hypothesized that the MR amplitudes on the night side are too small and contain EPB contributions, so they only discussed the dayside sector (6–18 LT). Here, we calculate the correlation coefficients between the MR amplitudes in each component and ionospheric conductivities with the data in all LT sectors. The R_{xy}, the correlation coefficient between Σ_{xy} and zonal components, is 0.96, and R_{yy}, the correlation coefficient between Σ_{yy} and meridional components, is 0.91; they both strongly support the hypothesis that the MR generation mechanism is the ionospheric dynamo.

For the small-amplitude MRs in the night side LT sector, the clear seasonal dependence is also observed on the night side (Fig. 4), almost identical to that on the day side (Fig. 2). The global distribution of the average MR amplitudes, as observed by SW-A on the night side, is almost identical to that observed by SW-C (Fig. 5), indicating
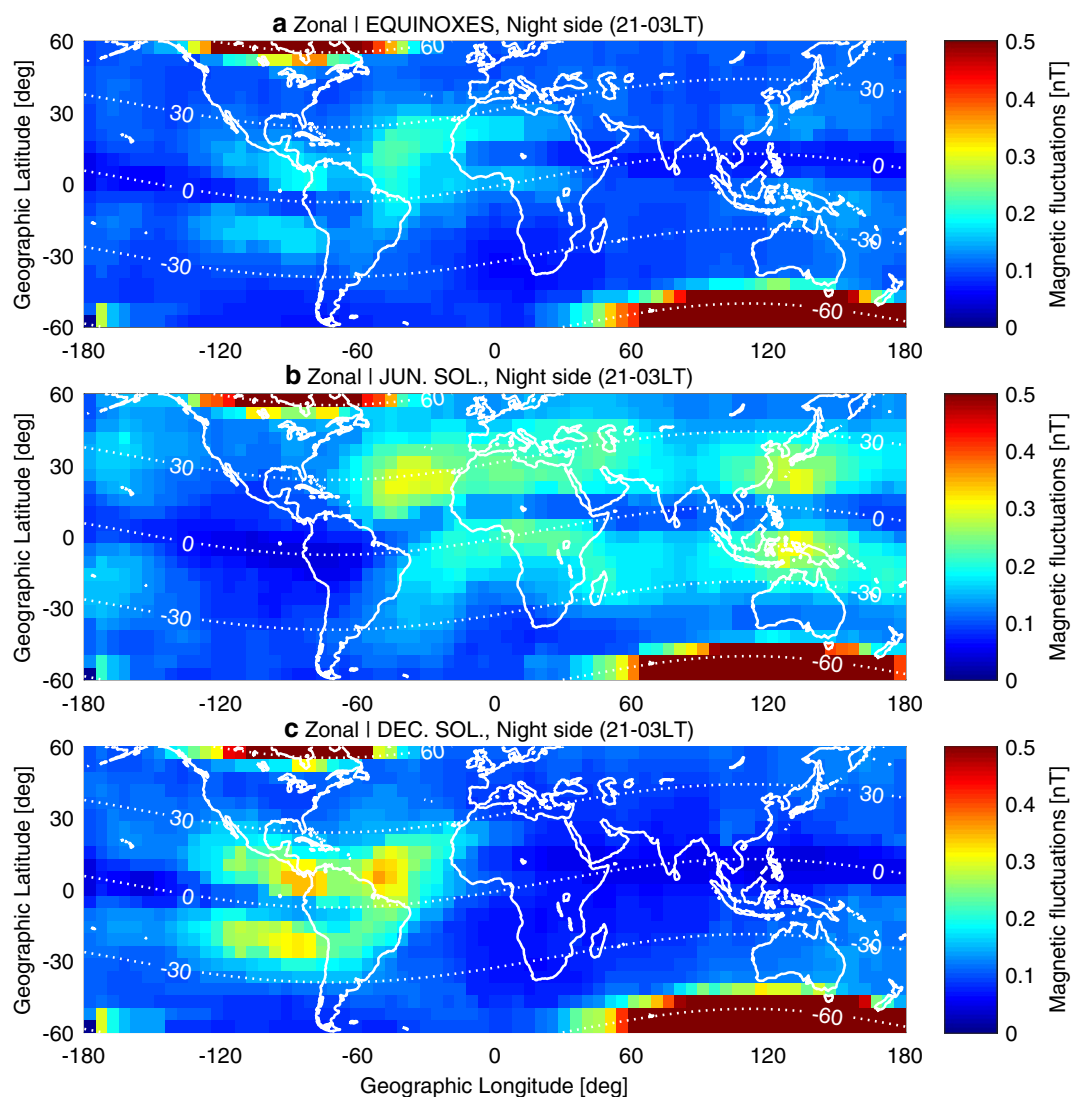

Fig. 3 LT dependence of the average amplitudes and two-dimensional ionospheric conductivities. The two-dimensional conductivities, Σ_{yy} and Σ_{xy}, are height-integrated from an altitude of 90–450 km at a location in Japan (33°N, 133°E) on April 2, 2015. *X* and *Y* indicate magnetic north and east, respectively. *Blue*, *red*, and *green lines* show the average amplitude of the MRs of the parallel, meridional, and zonal component between 30°N–35°N and 130°E–135°E, respectively. *Solid purple* and *dotted purple lines* show Σ_{yy} and Σ_{xy}, respectively

Aoyama *et al. Earth, Planets and Space* (2017) 69:89

Page 7 of 21

Fig. 4 Seasonal dependence of the MR amplitude distribution of the zonal component on the night side sector (21–3 LT). **a** Combined equinox, **b** June solstice and **c** December solstice

that the MRs on the night side LT sector are not instrumental noise but a real signal.

Amplitude difference between SW-A/SW-C and SW-B caused by their altitude difference

After April 17, 2014, SW-A/-C and SW-B were modified to fly at ~460 and ~510 altitudes, respectively. Figure 6 shows the amplitude distribution of the zonal components of the MRs on the dayside observed by each satellite, and the difference (i.e., subtraction) of the amplitudes of SW-B from those of SW-A. The figure for SW-C is not shown, but shows almost the same distribution as that of SW-A. We observe a difference in amplitude between SW-A and SW-B; for example, the maximum amplitude of SW-A around South America is

~0.7 nT, while that of SW-B flying ~50 km higher than SW-A and SW-C is ~0.6 nT, which is very small but statistically notable. The amplitude differences between the two Swarm satellites are larger at lower latitudes (Fig. 6c). From this statistical analysis, it is suggested that the origin of the MR amplitude difference between SW-A/SW-C and SW-B is not in the magnetosphere, but in the region below the SW-B altitude (about 520 km altitude). Possible explanations for the decreasing MR amplitudes at higher altitudes are as follows. First, the Pedersen current or polarization current short-circuited the FACs below the SW-B altitude because the Pedersen current tends to be larger at lower latitudes, and the polarization current is also proportional to electron density (and the rate of temporal variation in the electric
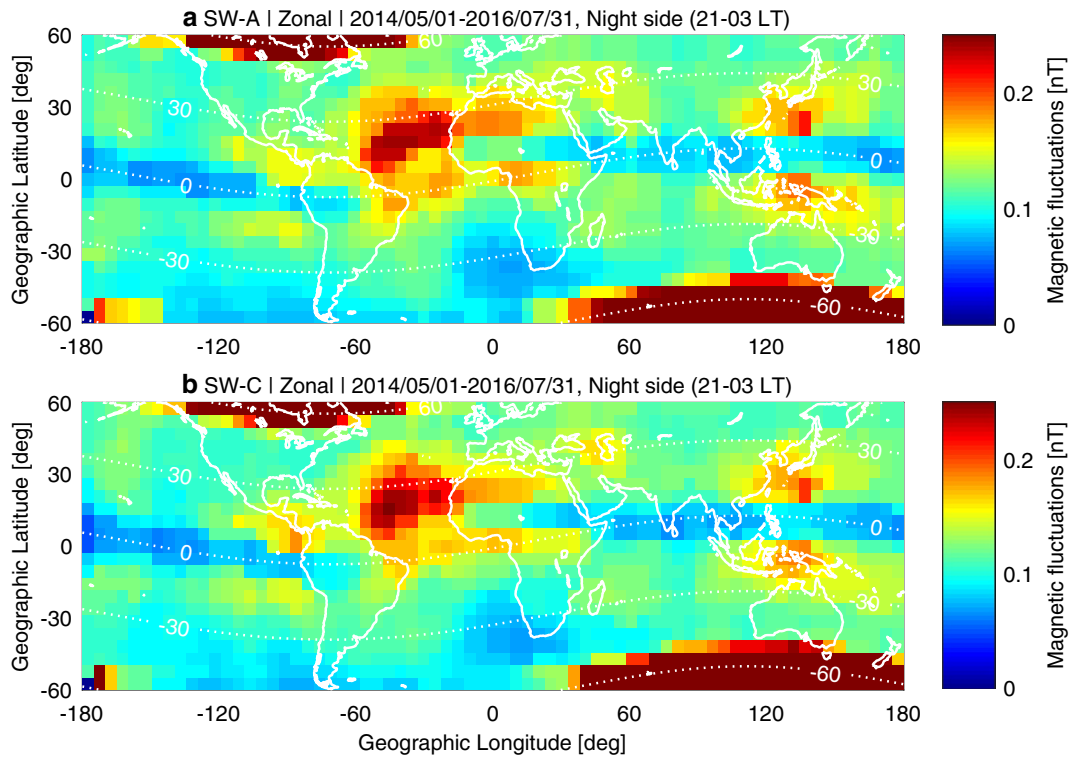
Aoyama *et al. Earth, Planets and Space* (2017) 69:89

Page 8 of 21

Fig. 5 Global distributions of the MR amplitudes of the zonal component on the night side (21–3 LT) observed by **a** SW-A and **b** SW-C within the time period, May 1, 2014–July 31, 2016

field). However, the contribution from polarization current may be negligible because the temporal variation must be slow enough for MRs to be regarded as spatial structures (Iyemori et al. 2015). Here, we roughly estimate the strength of the polarization and Pedersen currents. The polarization current j_p is given by

$$j_p \cong \frac{n_i m_i}{B_0^2} \frac{dE}{dt}, \tag{1}$$

where n_i is the ion number density, m_i is the ion mass, E is the electric field, and B_0 is the magnetic field strength.

If we assume

$$\frac{dE}{dt} \cong \frac{v \times B_0}{T}, \tag{2}$$

where v is the neutral velocity at the dynamo layer, and T is the wave period, the polarization current is estimated as $j_p \cong 3.8 \times 10^{-12}$ [A/m^2]. Here, we substituted the value of $n_i = 10^{11}$ [1/m^3], $m_i = 2.7 \times 10^{-26}$ [kg] he mass of an oxygen ion), $B_0 = 3 \times 10^{-5}$ [T], $v = 10$ [m/s], and $T = 240$ [s] in Eqs. (1) and (2). However, the Pedersen current $j_{Pedersen} = \sigma_p E = \sigma_p (v \times B_0)$ is calculated as $\sim 2.7 \times 10^{-10}$ [A/m^2]. Here, we substituted the value of $\sigma_p = 9.02 \times 10^{-7}$ [S/m]. Thus, we roughly estimate that $|j_p| \ll |j_{Pedersen}|$. In addition, the

height-integrated Pedersen conductivities from altitudes of 90–70 and 470–520 km at 12 LT on April 25, 2015 at a location of 33°N, 133°E are 1.501×10 [S] and 2.042×10^{-2} [S], respectively. 2.042×10^{-2} [S] is too small for a 10% difference in MR amplitude between SW-A/SW-C and SW-B. Second, the latitude of the footprint from a higher altitude to E-layer altitude (about 110 km) along the geomagnetic field-line increases, which indicates that the ionospheric conductivity and cumulus convection activity are weaker at higher latitudes. For example, at 12 LT on April 25, 2015 at location 25°N, 135°E, Σ_{xy} and Σ_{yy} at the footpoint of 470 and 520 km altitude are 2.893×10 [S] and 8.818 [S] and 2.738×10 [S] and 8.642 [S], respectively. That is, the effect of the difference in ionospheric conductivity is about 2–5%. The remainder may come from the latitudinal difference in cumulus convection activity, which is weaker at higher latitudes due to less solar radiation. The meridional components (not shown in this paper) observed by SW-A/SW-C are also larger than that from SW-B. The effect of height variation in the geomagnetic field is negligible and insufficient to explain the observed differences because, for example, the difference in geomagnetic intensity is only a few percent between the two heights although the amplitude difference is ≥10%.

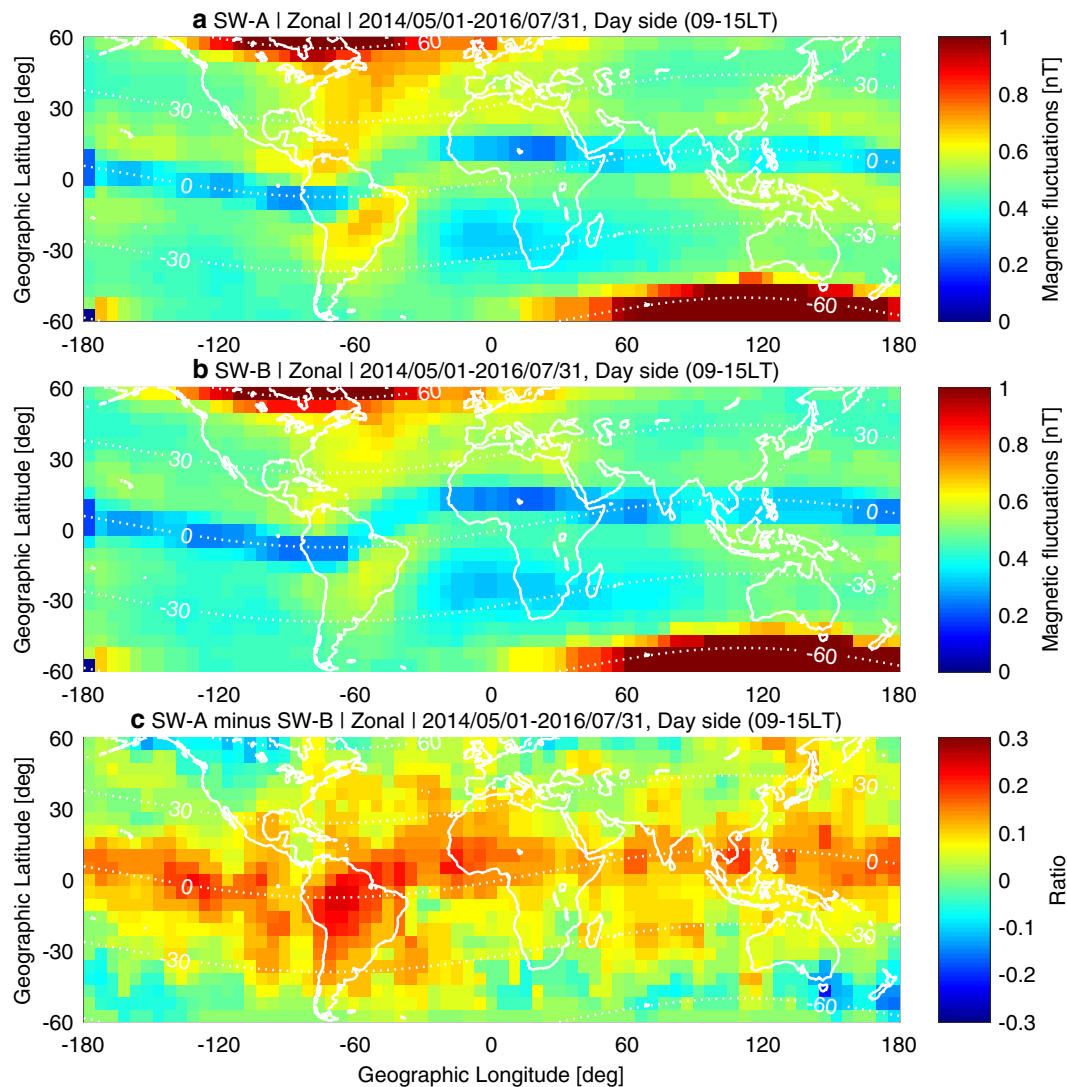Aoyama *et al. Earth, Planets and Space* (2017) 69:89

Page 9 of 21

Fig. 6 Difference in global distribution of the MRs between SW-A and SW-B. Global distribution of the MR amplitudes of the zonal component on the dayside (9–15 LT) as observed by **a** SW-A and **b** SW-B within the time period May 1, 2014–July 31, 2016. The *bottom panel* **c** shows the difference in amplitudes (SW-A minus SW-B) normalized with the amplitudes of SW-A in each grid

Results

Event analysis of MRs during typhoon activity

One of our main objectives is to show the relationship between MRs and typhoons. In this section, we investigate the amplitudes of the MRs above typhoons to verify their correlation.

A very strong typhoon no. 201408, NEOGURI, approached Japan on July 7, 2014 and struck the Japanese islands. From July 7 to July 11, the geomagnetic condition was rather quiet, for example, the $\sum Kp$ index was 11o, 12-, 14-, 14- and 11-, respectively, and the maximum Kp was 3o during this period. The Swarm satellites passed above the typhoon at 6 and 18 LT. Figure 7

shows the magnetic field fluctuations above the typhoon. Colored lines indicate the SW-A orbit (dotted line) and zonal component of the magnetic fluctuations (solid line), and stars indicate the location of the typhoon on each day when SW-A flew near the typhoon. The blue, orange, green, and purple lines correspond to each satellite path on July 8, 9, 10, and 11, respectively. The blank star in the southern hemisphere, dotted gray lines, and red lines indicate the conjugated point of the center of each typhoon in the northern hemisphere, the typhoon track, and dip equator, respectively. The amplitudes of the MRs during typhoon activity tend to be larger than those in non-typhoon areas, except for the paths on July
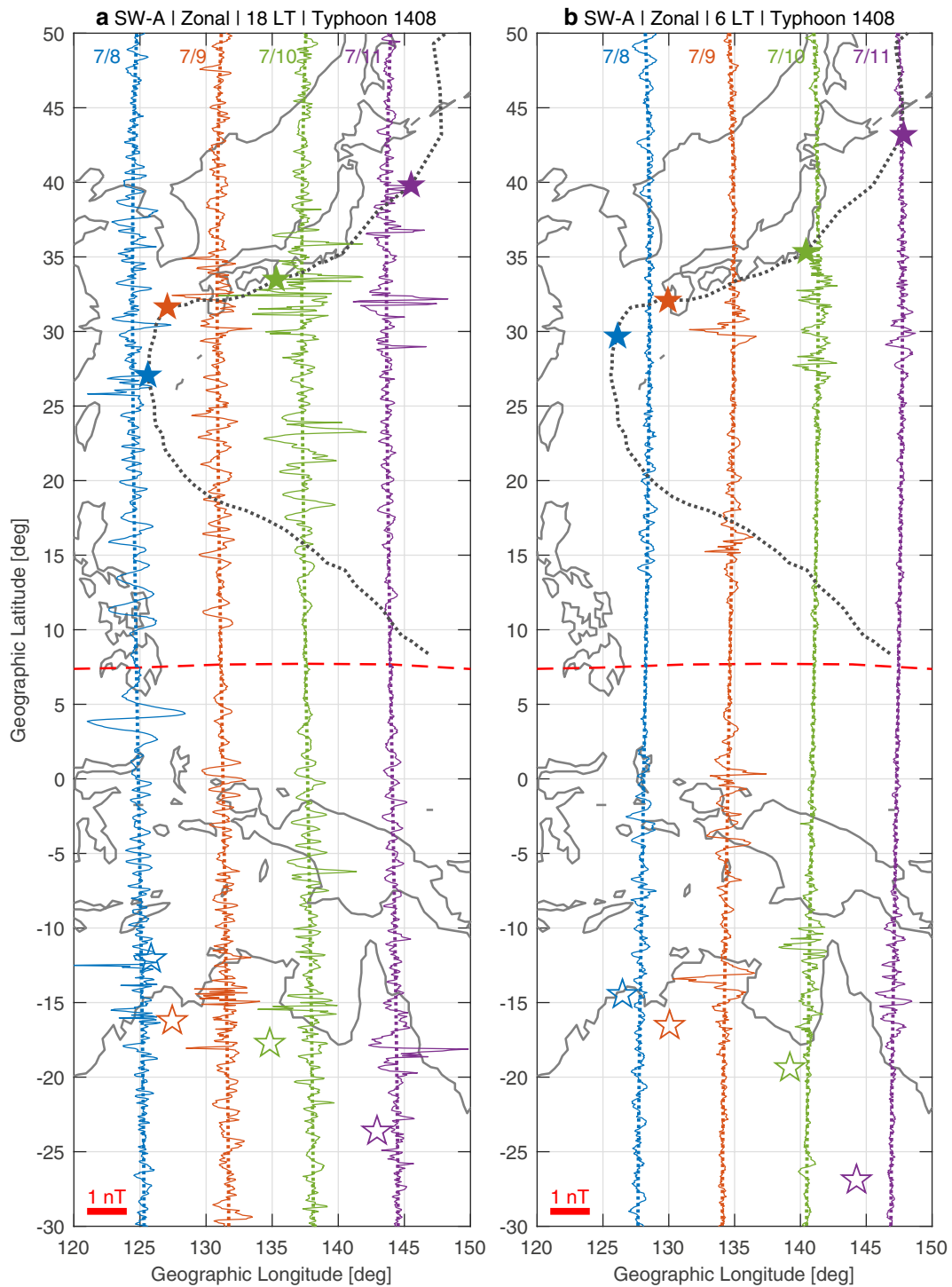
Aoyama *et al. Earth, Planets and Space* (2017) 69:89

Page 10 of 21

Fig. 7 MRs above typhoons as observed by SW-A. SW-A passed above the typhoon at **a** 18 LT and **b** 6 LT. *Colored lines* show the satellite orbit and zonal component of the magnetic fluctuations on each day; *blue, orange, green,* and *purple* correspond to July 8, 9, 10, and 11, 2014. *Stars, dotted gray lines,* and *red lines* indicate the location of the typhoon on each day, typhoon track, and dip equator. The *colors of the stars* correspond to the orbit with the *same color. Stars* in the southern hemisphere indicate the magnetic conjugated point of the location of the typhoon

Aoyama *et al. Earth, Planets and Space* (2017) 69:89

Page 11 of 21

8 and 11 at 6 LT. We interpret this tendency as the effect of typhoons, which generate acoustic waves and/or internal gravity waves that propagate to the ionospheric E and F layer and produce dynamo currents. Additionally, the location of a large amplitude event is almost the same when the satellite passes above the typhoon on the dusk side and 12 h later on the dawn side. This observation supports the hypothesis that lower atmospheric phenomena generate MR amplitude enhancements. Clear geomagnetic similarities in the amplitude enhancements are observed on all satellites paths, and this feature is almost always observed in both the event and statistical analyses (Figs. 1, 2, 4), regardless of typhoon existence. This indicates that these disturbances are from FACs.

Figure 8 shows IR cloud images plotted from IR brightness temperature data. We verify the relationship between the enhancements in MR amplitude and meteorological phenomena in the troposphere on each satellite path by comparing Figs. 6 and 7. First, there are neither clouds nor TCs below the enhancement region at higher latitudes in the southern hemisphere. Therefore, the amplitude enhancements in the southern hemisphere may be correlated with atmospheric disturbances in the northern hemisphere. An enhancement around 10°N–17°N (3°N–6°N in the southern hemisphere) on the blue path in Fig. 7a is shown. In Fig. 8a, a cloud elongates from the fringe of the typhoon to the southwest direction, where heavy rainfall is expected. Heavy rain accompanies the atmospheric disturbance, and the rain area may correspond to MR amplitude enhancements. Similarly, the amplitude enhancements around 17°N–25°N on July 8 at 18 LT, 28°N–33°N on July 11 at 18 LT, and 27°N–32°N on July 11 at 6 LT correspond to the cloud elongated from the typhoon. Note that the typhoon subsided to an extratropical cyclone on July 11 on the weather chart (not shown in this paper). During this typhoon event, most MR amplitude enhancements appeared to correspond to the lower atmospheric disturbance area associated with the typhoon. However, we should note that a typhoon does not continuously induce large amplitude MRs throughout its lifetime.

We show some typical examples of the correspondence between MRs and typhoons on the dawn side from August to October 2016 in Fig. 9. On the dawn side, the EPBs, which also generate a small-scale magnetic effect on their interior FACs, rarely occur. The solid green and blue indicate the total MR amplitudes, $\sqrt{(\delta B_X)^2 + (\delta B_Y)^2 + (\delta B_Z)^2}$ (where, $\delta B_X, \delta B_Y, \delta B_Z$: magnetic fluctuations in the sensor coordinate system). The locations of the typhoons centers are shown with yellow stars. Note that an elongated area of typhoons has a diameter of several hundred kilometers. The *Kp* index was 5+, 3−, 1+, 2+, 3o and 3+ during the period in

Fig. 9a–d, respectively. The total amplitudes of the MRs in Fig. 9a are much larger than those on other orbits in Fig. 9b at all latitudes, even taking into account the MR magnitudes dependence on LT. This could be an effect of a high *Kp* index. However, there is no reason that a high *Kp* should affect the MRs at certain latitudes. The enhancements in total MR amplitudes observed by both SW-A and SW-C are clearly observed at latitudes around the center of typhoons for all events in Fig. 9. The geomagnetic conjugacy is also observed, which means these MR disturbances are from FACs that remain for more than several tens of minutes (time for the satellites to fly from one hemisphere to another).

Statistical comparisons between MRs during typhoon and non-typhoon activities

In this section, we present a statistical analysis of typhoon events when the Swarm satellites flew close over the typhoons from November 26, 2013, to July 31, 2016. A total of 54 typhoons approached Japan in the period, as shown in Table 1. We selected the typhoon events used in our analyses as follows. The distance between the center of a typhoon and 5° × 5° mesh grid in the analysis area must have been <1000 km, which corresponds to the diameter of a typical typhoon. We also considered the seasonal dependence of the global distribution of MR amplitudes, as observed in Figs. 2 and 4. The maximum amplitude of the zonal component of MRs around East Asia on the day side (night side) in summer is ~0.7 (0.3) nT, but it drops to ~0.5 (0.1) nT in winter. In general, typhoons occur and encounter East Asia during summer to autumn. The EPBs appear at low magnetic latitudes after sunset to midnight and contribute to enhanced magnetic fluctuations (Stolle et al. 2006). The average amplitudes of MRs on the night side may contain the effect of the EPBs, and the occurrence rates of the EPBs around East Asia are high in autumn (see Stolle et al. 2006, Fig. 6). We use a weighted average of the MR amplitudes under the non-typhoon condition, $\bar{A}$, as follows to remove the contribution of the EPBs to the distribution of average MR amplitudes,

$$\bar{A} = \frac{\sum_{m=1}^{12} \bar{A}_m N_m}{\sum_{m=1}^{12} N_m}, \tag{3}$$

where $\bar{A}_m$ is the average MR amplitude of the non-typhoon grid in each month, N_m is the number of typhoon grids in each month, and the subscript m indicates the month.

The top and middle panels of Figs. 10, 11, 12 and 13 show the distribution of the weighted average MR amplitudes derived from Formula (3) in each component under non-typhoon conditions (left panel), and
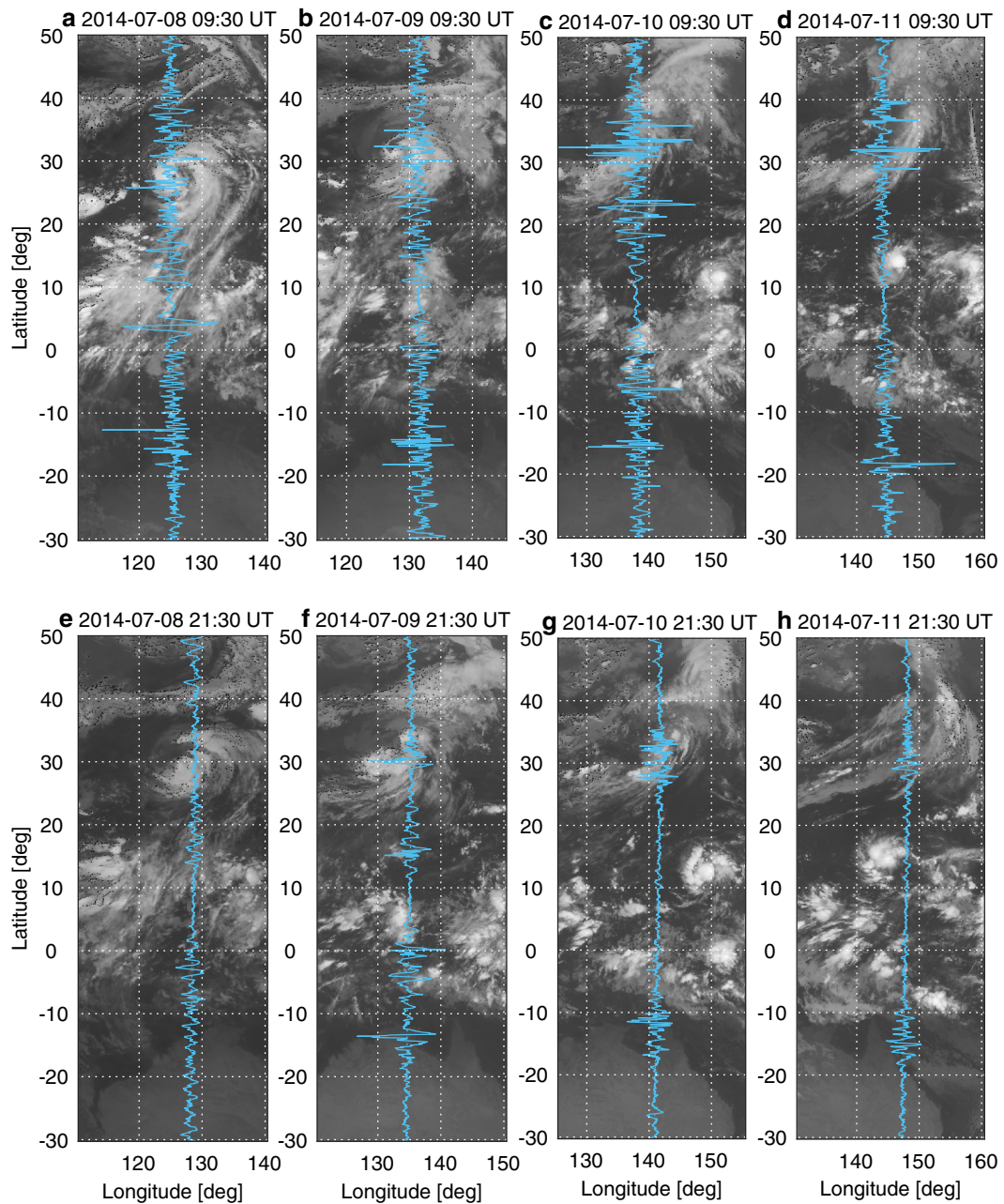
Aoyama *et al. Earth, Planets and Space* (2017) 69:89

Page 12 of 21

Fig. 8 IR cloud images plotted from IR brightness temperature data on each day. MRs are overlaid (*light blue solid lines*). *Upper* and *lower panels* are 18 and 6 LTs, respectively

normal average amplitudes during typhoon conditions (right) in each grid. The bottom panel in Figs. 10, 11, 12 and 13 shows the number of the satellite orbits under non-typhoon conditions (left) and typhoon conditions (right). The white indicates the area where there is no typhoon data. The average MR amplitudes below 20°N are extremely small because of the filtering effect near the dip equator, as discussed in Nakanishi et al. (2014). We

observe the following features in these figures. On the dawn side, the number of the data during the typhoon period is large in the region between 10°N–35°N and 120°E–160°E (bottom right panel of Fig. 10). The average MR amplitudes of the meridional component during typhoon are slightly larger than the non-typhoon period in the region between 15°N–45°N and 120°E–160°E (top panel of Fig. 10). The zonal components during typhoon
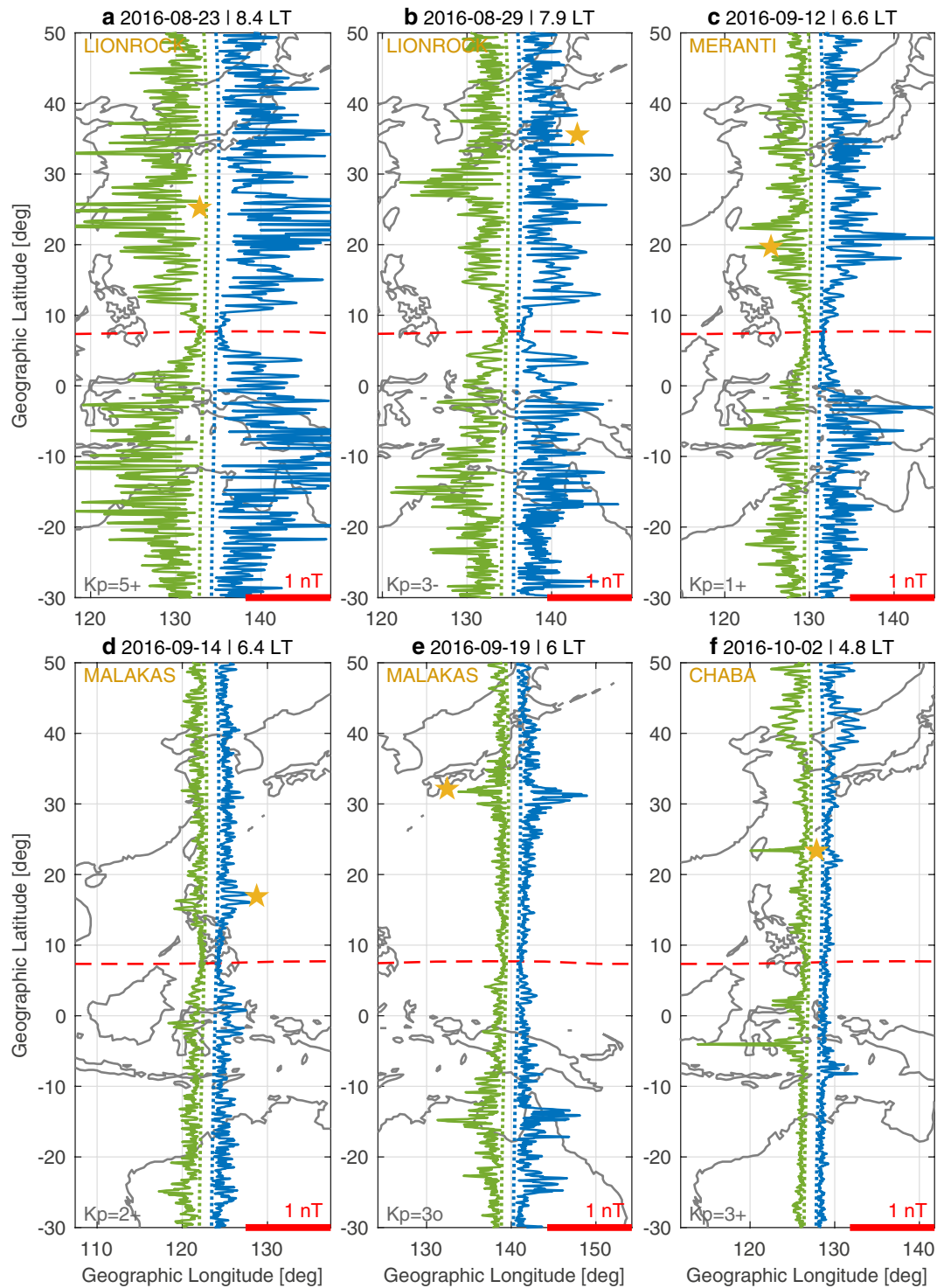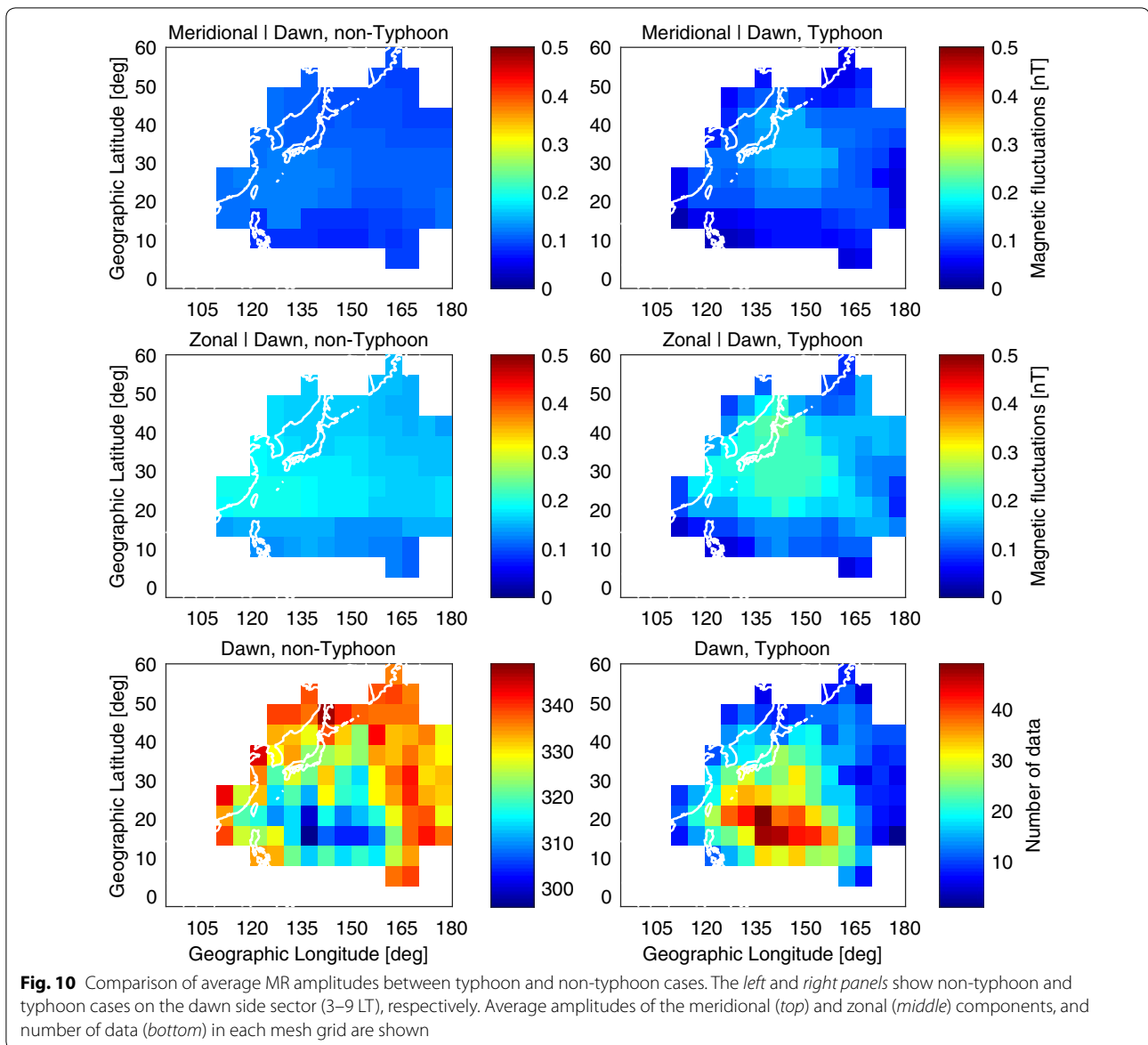
Aoyama *et al. Earth, Planets and Space* (2017) 69:89

Page 13 of 21

Fig. 9 Typical examples of the MRs during typhoon activity on the dawn (or morning) side simultaneously observed by both SW-A and SW-C. The *solid green* and *blue*, and *dotted green* and *blue lines* indicate total MR amplitudes from SW-A and SW-C, and orbits of the SW-A and SW-C, respectively. The *yellow stars* and *dotted red lines* indicate the center of the typhoons and dip equator, respectively

Fig. 10 Comparison of average MR amplitudes between typhoon and non-typhoon cases. The *left* and *right panels* show non-typhoon and typhoon cases on the dawn side sector (3–9 LT), respectively. Average amplitudes of the meridional (*top*) and zonal (*middle*) components, and number of data (*bottom*) in each mesh grid are shown

are apparently larger in the region between 15°N–45°N and 120°E–160°E (middle panel of Fig. 10). Both of these regions overlap with the typhoon area. On the day side, the number of data during the typhoon period is large in the region between 10°N–35°N and 120°E–160°E (bottom right panel of Fig. 11). The average MR amplitudes of the meridional component during the typhoon period are larger than the non-typhoon period in the regions between 25°N–30°N and 105°E–110°E and 35°N–40°N and 125°E–140°E (top panel of Fig. 11), but there is a very small number of data during the typhoon period in these regions. The zonal component during the typhoon period is larger in the region between 25°N–40°N and 125°E–140°E (middle panel of Fig. 11), and this region overlaps with the typhoon area. On the dusk side, the

number of data during the typhoon period is large in the region between 10°N–40°N and 120°E–160°E (bottom right panel of Fig. 12). Both the meridional and zonal components are enhanced along the Japan island arc, and these regions overlap with the typhoon area. On the night side, the number of the data during the typhoon period is large in the region between 10°N–35°N and 115°E–160°E (bottom right panel of Fig. 13). The average MR amplitudes of the meridional component during the typhoon period are larger than the non-typhoon period in the region between 20°N–40°N and 110°E–135°E (top panel of Fig. 13). The zonal component during the typhoon period is larger in the region between 20°N–35°N and 110°E–150°E (middle panel of Fig. 13). Both of these regions overlap with the typhoon area. In summary, on
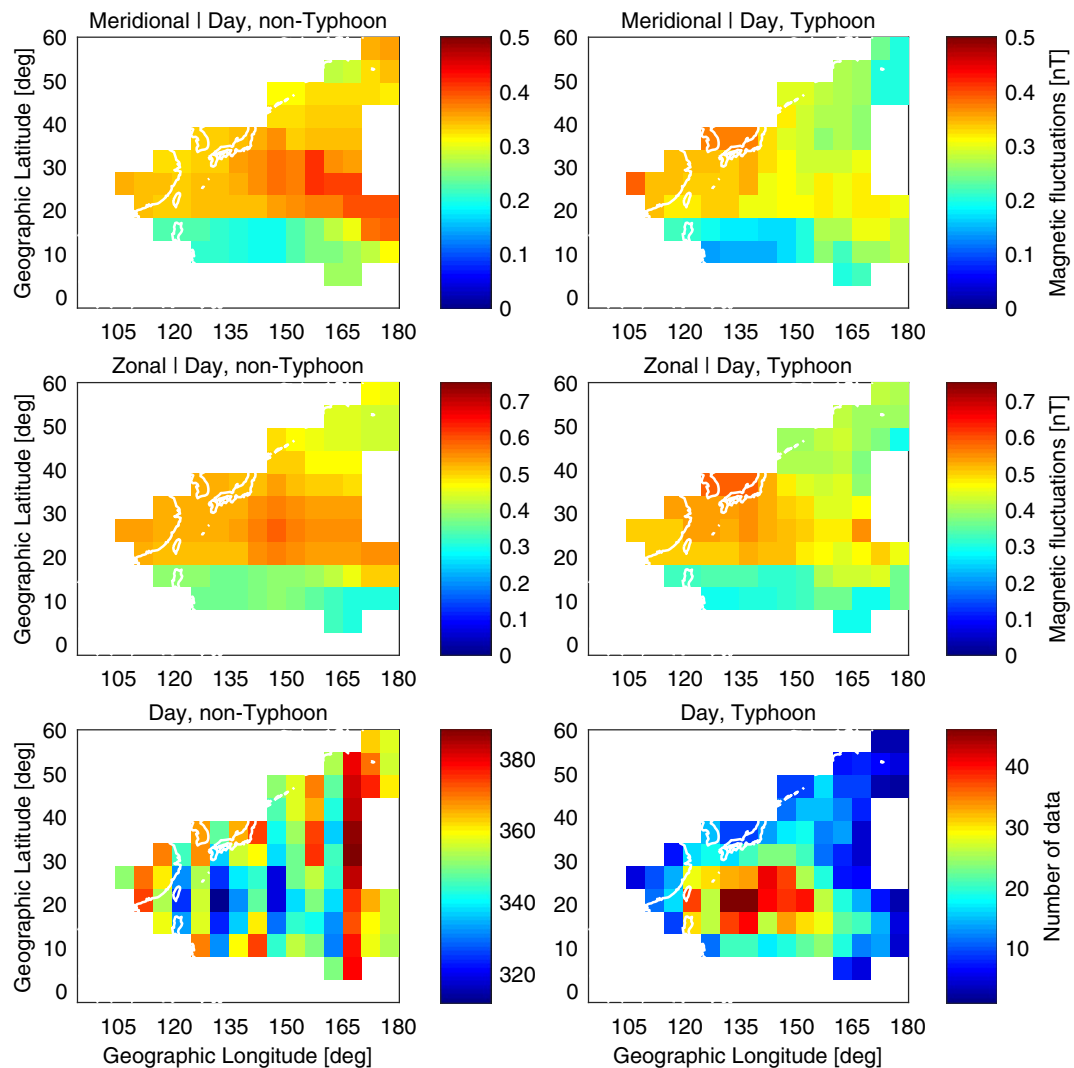
Aoyama *et al. Earth, Planets and Space* (2017) 69:89

Page 15 of 21

Fig. 11 Comparison of average MR amplitudes between typhoon and non-typhoon cases. The *left* and *right panels* show non-typhoon and typhoon cases on the day side sector (9–15 LT), respectively. Average amplitudes of the meridional (*top*) and zonal (*middle*) components, and number of data (*bottom*) in each mesh grid are shown

the day side sector, the average amplitudes under non-typhoon conditions are larger than those under typhoon conditions in many grids, although there are a few grids between 25°N–40°N and 125°E–140°E where the average MR amplitudes during typhoon conditions are larger than those under non-typhoon conditions (Fig. 11). In most grids between 20°N–35°N and 120°E–150°E, where there are enough data, the average MR amplitudes during typhoon activity are larger than those above the non-typhoon areas on the dawn side (Fig. 10), dusk side (Fig. 12), and night side (Fig. 13) sectors. On the dusk side (Fig. 12), an amplitude enhancement of the typhoon grids in both components is observed along the Japan island arc, where typhoons tend to move along.

We performed a *t* test at the 5% significance level to determine the significance of the average amplitude differences between the typhoon and non-typhoon periods. Because of the filtering effect discussed in Nakanishi et al. (2014), the amplitude decreases at latitudes lower than about 15°. Therefore, we limit the area of the *t* test to between 20°N–35°N and 120°E–140°E, see Figs. 1, 2, and 4. For the average amplitude difference between the typhoon and non-typhoon periods in this region, the amplitude of typhoon periods is larger than that of the non-typhoon periods, except for the meridional component on the day side. The results of the *t* test are summarized in Table 2. "Yes" indicates a significant difference between the typhoon and non-typhoon average

Aoyama *et al. Earth, Planets and Space* (2017) 69:89
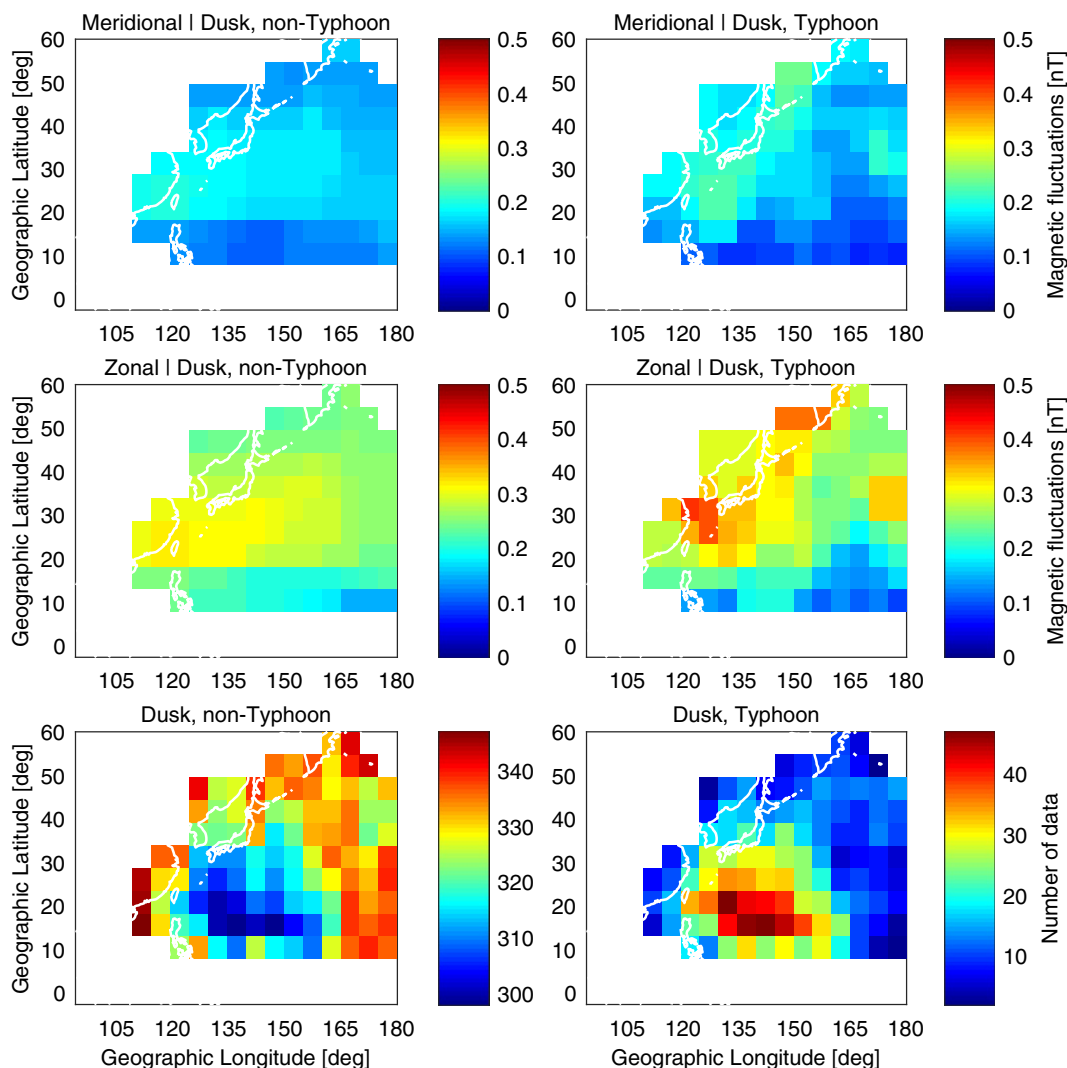
Page 16 of 21

Fig. 12 zMR amplitudes between typhoon and non-typhoon cases. The *left* and *right panels* show non-typhoon and typhoon cases on the dusk side sector (15–21 LT), respectively. Average amplitudes of the meridional (*top*) and zonal (*middle*) components, and number of data (*bottom*) in each mesh grid are shown

amplitude was recognized. We should note that at least half the results (cases) show the existence of a significant difference, although the other half does not.

The possible reason for the lack of clear difference is that non-typhoon activities include low pressures activity, which can be sources of acoustic and/or gravity waves. The t test results shows that a significant difference is not always observed, especially not on the day side sector. A plausible reason is that cumulus convection activity on the day side is enhanced by solar radiation, which is discussed below.

Discussion

One primary objective of this paper is to show new evidence that demonstrates the connection between MRs and lower atmospheric disturbances using tropical cyclone activity. Aoyama et al. (2016) reported simultaneous observations of TEC, satellite, and ground magnetic fields indicating that the 2015 eruption of Chile's Calbuco volcano induced a vertical acoustic resonance between the ionospheric E-layer and the ground. Furthermore, a Swarm satellite observed the magnetic effect of an FAC generated through the E-layer dynamo. In this
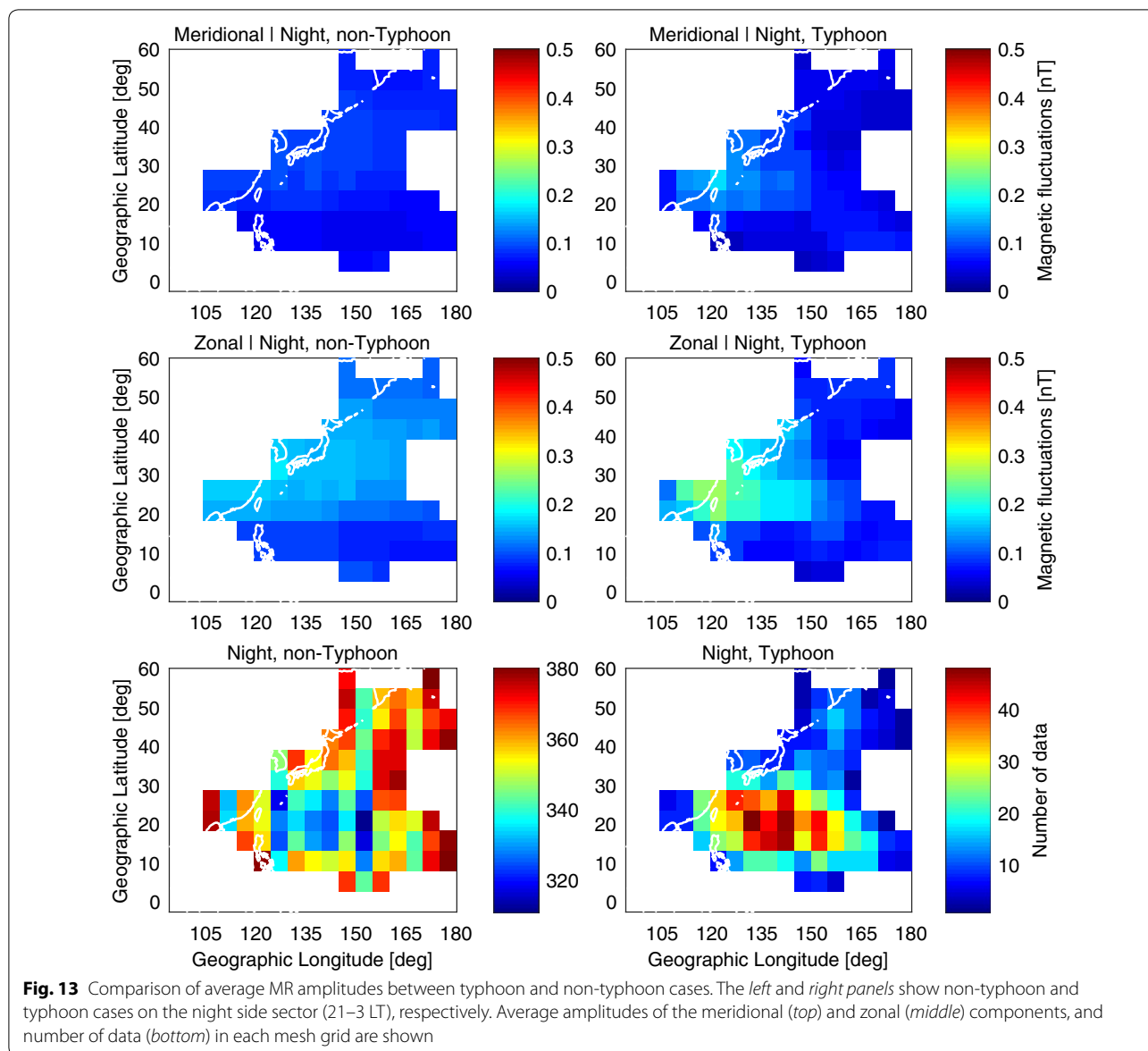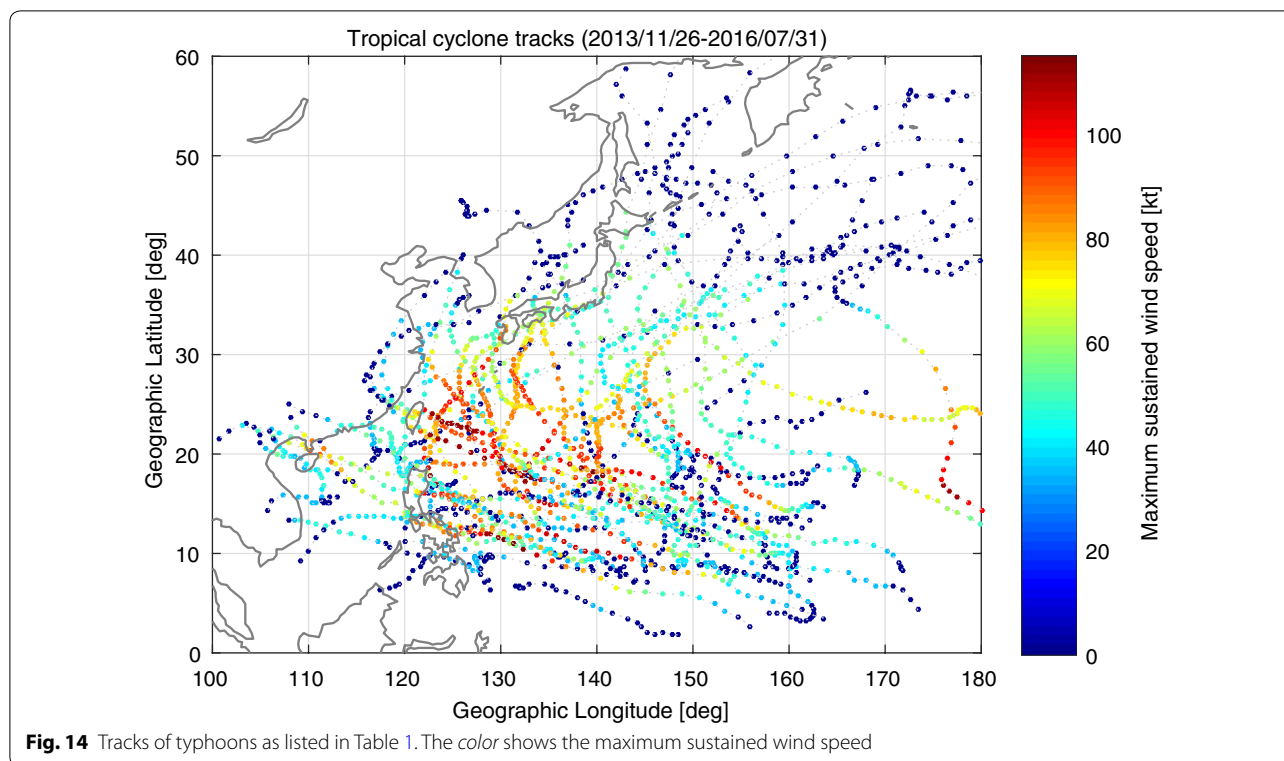
Aoyama *et al. Earth, Planets and Space* (2017) 69:89

Page 17 of 21

Fig. 13 Comparison of average MR amplitudes between typhoon and non-typhoon cases. The *left* and *right panels* show non-typhoon and typhoon cases on the night side sector (21–3 LT), respectively. Average amplitudes of the meridional (*top*) and zonal (*middle*) components, and number of data (*bottom*) in each mesh grid are shown

Table 2 Results of the *t* tests for significance of amplitude differences

	Meridional component	Zonal component
Dawn side	No	Yes
Day side	No	No
Dusk side	No	Yes
Night side	Yes	Yes

study, we investigated northern hemisphere typhoons that occurred around the western Pacific Ocean.

From the event analyses described in "Event analysis of MRs during typhoon activity", typhoons seem to have a

close relationship with MRs. Figure 14 shows the typhoon tracks for the period from November 26, 2013, to July 31, 2016, as listed in Table 1. The red colors indicate higher wind speed. The statistical analysis performed in "Statistical comparisons between MRs during typhoon and non-typhoon activities" indicates that the number of data with typhoons at each grid point is large between 15°N–35°N and 120°E–160°E ("typhoon area"), where storms develop into a strong typhoons (Fig. 14). As the event analyses performed in this study has shown, MR activity is generally correlated with typhoon activity. However, cases showing a lack of MR enhanced strength during typhoons and enhancement during the non-typhoon period exist. Therefore, we have to consider the region where the

Aoyama *et al. Earth, Planets and Space* (2017) 69:89

Page 18 of 21

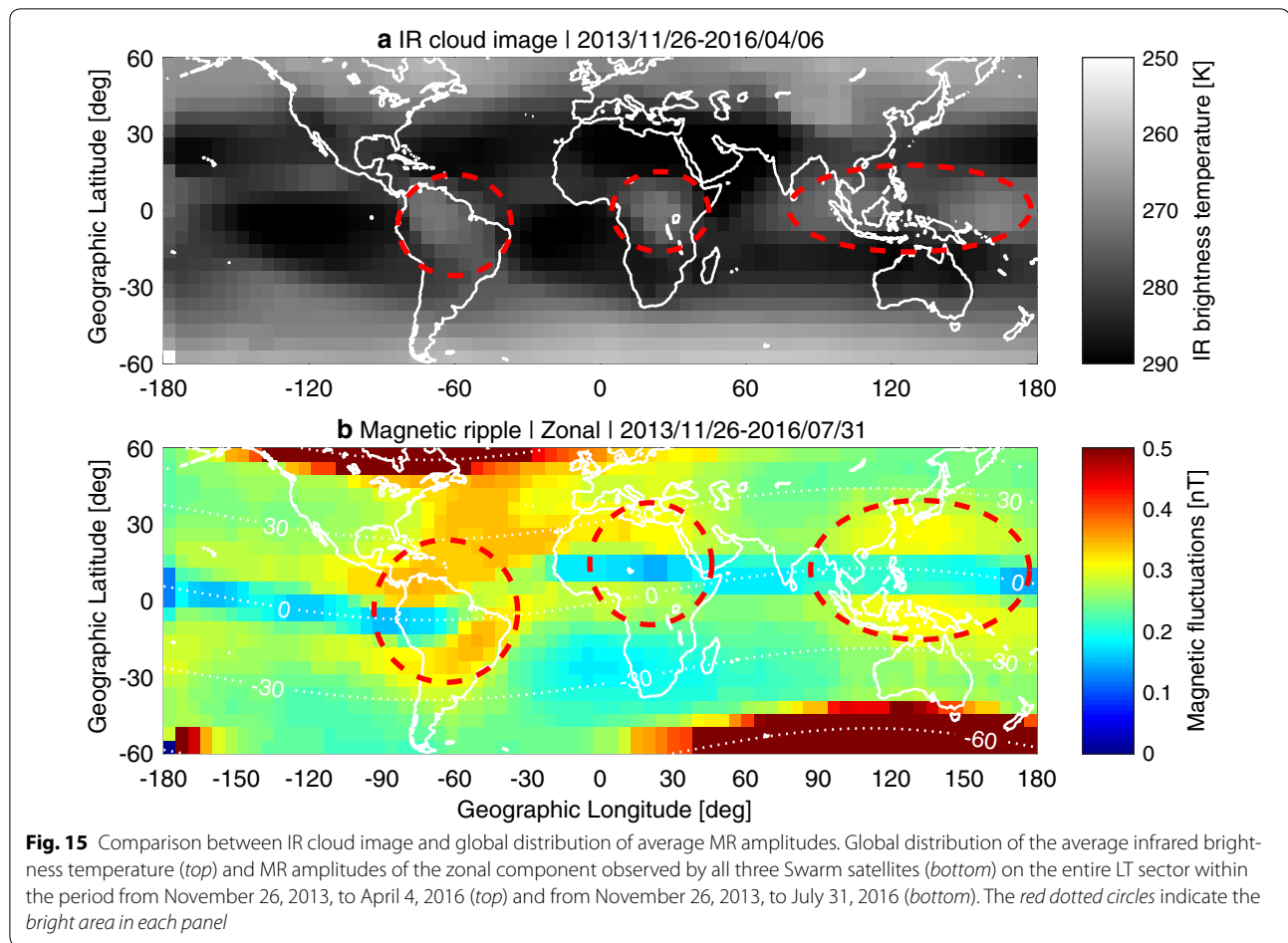**Fig. 14** Tracks of typhoons as listed in Table 1. The *color* shows the maximum sustained wind speed

number of data for the typhoon period (bottom right panel in Figs. 10, 11, 12 and 13) is large enough (>30); note that number of data for the typhoon period is large in the typhoon area. The average MR amplitudes in both the meridional and zonal component under typhoon conditions are, in general, larger than those in the non-typhoon case in the "typhoon area" (see Figs. 10, 12, 13). For the dusk and night sides, the area of enhanced amplitude is along the Japanese island arc in addition to the typhoon area, although such characteristics are not clear on the day side (Fig. 11). The cumulus convection activity increases during the day time because updrafts originate from the ground or sea surface heated from solar radiation, while the typhoon activity is almost the same during both day and night. Assuming the background amplitudes of the MRs are mainly generated from cumulus convection, we can explain the clear correspondence between the MRs and typhoons on the night side.

As described previously, we have shown the relationship between MRs and lower atmospheric disturbances including typhoons. However, we have not shown which types of waves, i.e., acoustic waves or gravity waves, cause the MRs. Iyemori et al. (2015) estimated the temporal scale of variation in MRs and suggested that they are most likely due to acoustic waves, although the data period they used does not include typhoons. According to the statistical analysis in Matsumura et al. (2010),

a high occurrence rate of spectral peaks in atmospheric pressure perturbations is found around the theoretical period of vertical acoustic resonance between the ground and ionosphere in the typhoon season (August–October). Chen et al. (2014) reported that acoustic waves from upward air motion during typhoons triggered magnetic disturbances in the period band between 143 and 400 s. To determine the type of wave that generates MRs from the data set used in this study, more analysis is necessary. For example, simultaneous observations of TEC, ground magnetic field, micro-barometric, and HF Doppler shift observations should be conducted to identify the waves by their period.

The relationship, lack thereof, between the MR and lower atmospheric disturbance needs to be addressed. On the night side, maximum amplitudes of the MRs are roughly recorded above the ocean (Figs. 1d, 4), while those on the day side are recorded above the continent (Figs. 1b, 2). This may be due to the difference in specific heat capacity between water (i.e., ocean) and rock (i.e., continent). That is, a continent is heated from solar radiation and convection activity over the continent becomes larger than that over the ocean on the day side. Meanwhile, the activity at night remains over the ocean and is lost over the continent.
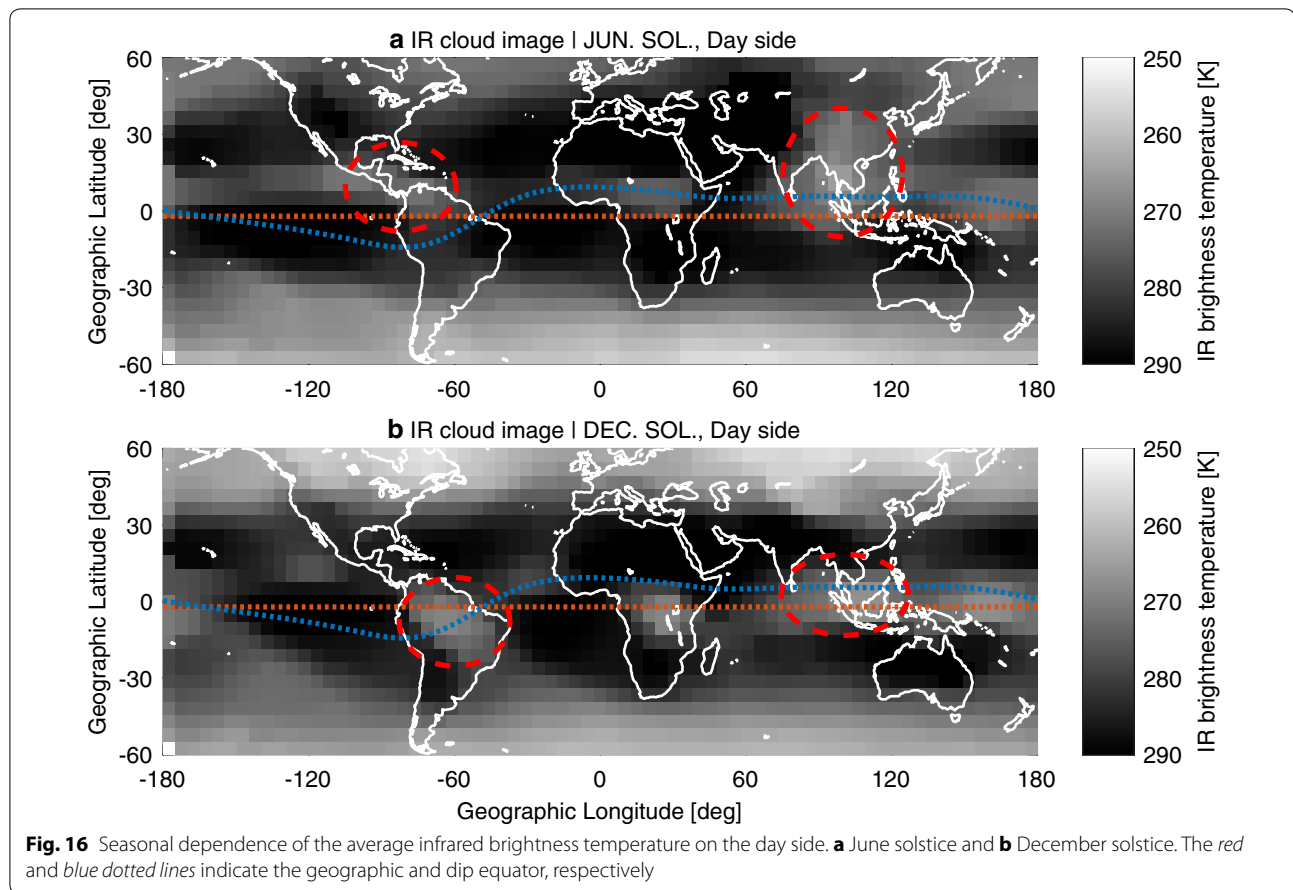
Figure 15a shows convection activity in the troposphere averaged from November 26, 2013, to April 6, 2016. The

Aoyama *et al. Earth, Planets and Space* (2017) 69:89

Page 19 of 21

Fig. 15 Comparison between IR cloud image and global distribution of average MR amplitudes. Global distribution of the average infrared brightness temperature (*top*) and MR amplitudes of the zonal component observed by all three Swarm satellites (*bottom*) on the entire LT sector within the period from November 26, 2013, to April 4, 2016 (*top*) and from November 26, 2013, to July 31, 2016 (*bottom*). The *red dotted circles* indicate the *bright area in each panel*

IR brightness temperature data are used as a proxy for convection activity and are available every 30 min at a spatial resolution of 4 km until April 6, 2016. The data are averaged in a mesh grid of 5° × 5° in geographic latitude and longitude to compare the convection activity with the MR distribution. A 3 × 3 pixel median filter has been applied to the image to smooth it. The three bright areas, i.e., the northern area of South America, the middle areas of Africa and South East Asia–Oceania region, are shown at low latitude (red dotted circles in Fig. 15a). Figure 15b presents the average MR amplitudes of the zonal component on all LT sectors from November 26, 2013, to July 31, 2016 derived from all three Swarm satellites. The bright areas of the MRs (red dotted circles in Fig. 15b) are almost at the same longitudes as the IR bright areas, i.e., lower temperature, which indicates the location of a higher cloud top caused by the strong convection in the troposphere. Figure 16 presents global distributions of the average IR brightness temperature in each bin within each season, in the same format as Fig. 15a. In the American (100°W–80°W) and Asian (80°E–100°E) sectors, the

bright areas (red dotted circles) move to northward in the June solstice while southward in the December solstice. These bright areas in June are located ~15° in latitude away from the dip equator. This may be the explanation for large MR amplitudes above the South American Continent and East Asia/Oceania during the June solstice on the day side (Fig. 2b). In contrast, in the African sector (10°E–40°E), the bright areas in both June and December solstice are not away more than ~ 15° in latitude from the dip equator. The source near the dip equator does not affect the MRs because the geomagnetic field-line near the dip equator at the altitude of the ionospheric E-layer does not reach the satellite altitudes. Taking into account the filtering effect around the dip equator (±~5°), it is necessary that the source is located ~14.6° in latitude away from the dipole equator.

Hoffmann et al. (2013) reported global distributions of gravity waves in the stratosphere from space-borne data. The hotspots of stratospheric gravity waves can roughly explain the bright areas of MR distribution for North America and East Asia in the June solstice, and Brazil in

Fig. 16 Seasonal dependence of the average infrared brightness temperature on the day side. **a** June solstice and **b** December solstice. The *red* and *blue dotted lines* indicate the geographic and dip equator, respectively

the December solstice, but the hotspot in southern Chile is not observed in MR amplitudes (see Fig. 6a, c in Hoffmann et al. 2013 and Fig. 2b, c in this paper).

Summary and conclusion

From the event analysis of typhoon No. 201408, enhanced MR amplitudes were often seen above the typhoon, but not always. Furthermore, the cloud arm from the typhoon appears to be related to the MR amplitude enhancement. From statistical analysis, the average amplitudes on the dawn side, dusk side, and night side are clearly larger above the typhoon area than those under the non-typhoon period, especially at the area where typhoons have developed; however, differences in amplitude are not very clear on the dayside. Additionally, according to the *t* test, a significant difference between the typhoon and non-typhoon period was recognized in the average amplitudes of the zonal component on the dawn and dusk side and the meridional and zonal component on the night side. The more complex day side relationship could be explained as due to relatively large effects of enhanced convective motion on the day side; that is, MR activity is consistently enhanced due to active dayside convection, and correlations with typhoon activity cannot be statistically isolated. Based on the event and statistical analyses, we conclude that the typhoon activity is correlated with MR activity and MRs without typhoon activity possibly originate from cumulus convection with higher activity on the day side.

Authors' contributions
TA analyzed the Swarm satellite and typhoon best track data and drafted the manuscript. TI participated in the design of the study and helped draft the manuscript. KN participated in the discussion of the results. All authors read and approved the final manuscript.

Aoyama *et al. Earth, Planets and Space* (2017) 69:89

Page 21 of 21

References

Akiya Y, Saito A, Sakanoi T et al (2014) First spaceborne observation of the entire concentric airglow structure caused by tropospheric disturbance. Geophys Res Lett 41:6943–6948. doi:10.1002/2014GL061403

Aoyama T, Iyemori T, Nakanishi K et al (2016) Localized field-aligned currents and 4-min TEC and ground magnetic oscillations during the 2015 eruption of Chile's Calbuco volcano. Earth Planets Space 68:148. doi:10.1186/s40623-016-0523-0

Bilitza D, Altadill D, Zhang Y et al (2014) The International Reference Ionosphere 2012—a model of international collaboration. J Space Weather Space Clim 4:A07. doi:10.1051/swsc/2014004

Chen C-H, Wang C-H, Lin L-C et al (2014) Typhoon-induced magnetic disturbances: cases in the western Pacific. Terr Atmos Ocean Sci 25:647–653. doi:10.3319/TAO.2014.05.08.01(AA)

Dhaka SK (2003) Gravity wave generation in the lower stratosphere due to passage of the typhoon 9426 (Orchid) observed by the MU radar at Shigaraki (34.85°N, 136.10°E). J Geophys Res 108:4595. doi:10.1029/2003JD003489

Hoffmann L, Xue X, Alexander MJ (2013) A global view of stratospheric gravity wave hotspots located with atmospheric infrared sounder observations. J Geophys Res Atmos. doi:10.1029/2012JD018658

Huang Y-N, Cheng K, Chen S-W (1985) On the detection of acoustic-gravity waves generated by typhoon by use of real time HF Doppler frequency shift sounding system. Radio Sci 20:897–906. doi:10.1029/RS020i004p00897

Ishii M, Sugiura M, Iyemori T, Slavin JA (1992) Correlation between magnetic and electric field perturbations in the field-aligned current regions deduced from DE 2 observations. J Geophys Res 97:13877–13887. doi:10.1029/92JA00110

Iyemori T, Ikeda T, Nakagawa A (1985) Amplitude distribution of small-scale magnetic fluctuations over the polar ionosphere observed by Magsat. J Geophys Res 90:335–339

Iyemori T, Nose M, Han D et al (2005) Geomagnetic pulsations caused by the Sumatra earthquake on December 26, 2004. Geophys Res Lett 32:1–4. doi:10.1029/2005GL024083

Iyemori T, Tanaka Y, Odagi Y et al (2013) Barometric and magnetic observations of vertical acoustic resonance and resultant generation of field-aligned current associated with earthquakes. Earth Planets Space. doi:10.5047/eps.2013.02.002

Iyemori T, Nakanishi K, Aoyama T et al (2015) Confirmation of existence of the small-scale field-aligned currents in middle and low latitudes and an estimate of time scale of their temporal variation. Geophys Res Lett 42:22–28. doi:10.1002/2014GL062555

Lühr H, Park J, Gjerloev JW et al (2015) Field-aligned currents' scale analysis performed with the Swarm constellation. Geophys Res Lett 42:1–8. doi:10.1002/2014GL062453

Matsumura M, Iyemori T, Nose M et al (2010) The predominant periods of the atmospheric perturbations and geomagnetic oscillations. Sol Terr Sci 21:129–142

Nakanishi K, Iyemori T, Taira K, Lühr H (2014) Global and frequent appearance of small spatial scale field-aligned currents possibly driven by the lower atmospheric phenomena as observed by the CHAMP satellite in middle and low latitudes. Earth Planets Space 66:40. doi:10.1186/1880-5981-66-40

Olsen N, Friis-christensen E, Floberghagen R et al (2013) The Swarm Satellite Constellation Application and Research Facility (SCARF) and Swarm data products. Earth Planets Space 65:1189–1200. doi:10.5047/eps.2013.07.001

Park J, Lühr H, Stolle C et al (2009) The characteristics of field-aligned currents associated with equatorial plasma bubbles as observed by the CHAMP satellite. Ann Geophys 27:2685–2697. doi:10.5194/angeo-27-2685-2009

Park J, Lühr H, Kervalishvili G et al (2015) Nighttime magnetic field fluctuations in the topside ionosphere at midlatitudes and their relation to medium-scale traveling ionospheric disturbances: the spatial structure and scale sizes. J Geophys Res Space Phys 120:6818–6830. doi:10.1002/2015JA021315

Picone JM, Hedin AE, Drob DP, Aikin AC (2002) NRLMSISE-00 empirical model of the atmosphere: statistical comparisons and scientific issues. J Geophys Res Space Phys 107:1–16. doi:10.1029/2002JA009430

Polyakova AS, Perevalova NP (2011) Investigation into impact of tropical cyclones on the ionosphere using GPS sounding and NCEP/NCAR reanalysis data. Adv Space Res 48:1196–1210. doi:10.1016/j.asr.2011.06.014

Polyakova AS, Perevalova NP (2013) Comparative analysis of TEC disturbances over tropical cyclone zones in the North-West Pacific Ocean. Adv Space Res 52:1416–1426. doi:10.1016/j.asr.2013.07.029

Rozhnoi A, Solovieva M, Levin B et al (2014) Meteorological effects in the lower ionosphere as based on VLF/LF signal observations. Nat Hazards Earth Syst Sci 14:2671–2679. doi:10.5194/nhess-14-2671-2014

Saito A, Iyemori T, Sugiura M et al (1995) Conjugate occurrence of the electric field fluctuations in the nighttime midlatitude ionosphere. J Geophys Res 100:21439–21451

Saryo T, Takeda M, Araki T et al (1989) A midday bite-out event of the F2-layer observed by MU radar. J Geomagn Geoelectr 41:727–734. doi:10.1089/ten.TEA.2016.0230

Sato K (1993) Small-scale wind disturbances observed by the MU radar during the passage of typhoon kelly. J Atmos Sci 50:518–537

Stolle C, Lühr H, Rother M, Balasis G (2006) Magnetic signatures of equatorial spread F as observed by the CHAMP satellite. J Geophys Res 111:A02304. doi:10.1029/2005JA011184

Sugiura M, Maynard NC, Farthing WH et al (1982) Initial results on the correlation between the magnetic and electric fields observed from the DE-2 satellite in the field-aligned current regions. Geophys Res Lett 9:985–988

Suzuki S, Vadas SL, Shiokawa K et al (2013) Typhoon-induced concentric airglow structures in the mesopause region. Geophys Res Lett 40:5983–5987. doi:10.1002/2013GL058087

Xiao Z, Xiao SG, Hao YQ, Zhang DH (2007) Morphological features of ionospheric response to typhoon. J Geophys Res Space Phys 112:1–5. doi:10.1029/2006JA011671

Yue J, Miller SD, Hoffmann L, Straka WC (2014) Stratospheric and mesospheric concentric gravity waves over tropical cyclone Mahasen: Joint AIRS and VIIRS satellite observations. J Atmos Solar-Terr Phys 119:83–90

Zettergren MD, Snively JB (2013) Ionospheric signatures of acoustic waves generated by transient tropospheric forcing. Geophys Res Lett 40:5345–5349. doi:10.1002/2013GL058018

Zettergren MD, Snively JB (2015) Ionospheric response to infrasonic-acoustic waves generated by natural hazard events. J Geophys Res A Space Phys 120:8002–8024. doi:10.1002/2015JA021116

Zettergren MD, Snively JB, Komjathy A, Verkhoglyadova OP (2017) Nonlinear ionospheric responses to large-amplitude infrasonic-acoustic waves generated by undersea earthquakes. J Geophys Res Space Phys. doi:10.1002/2016JA023159